This paper has been submitted to the Journal of Glaciology and is currently under review. Subsequent versions of this manuscript may have slightly different content. If accepted, the manuscript will be updated and the DOI of the accepted paper will appear on the 'Peer-reviewed Publication DOI' link on the right-hand side of this webpage. Please feel free to contact any of the authors; we welcome feedback.

A Markov chain Monte Carlo approach for geostatistically simulating mass-conserving subglacial topography

Niya SHAO,[1] Emma J MACKIE,[1] Michael J FIELD,[1] Felicity S MCCORMACK[2]

[1]*Department of Geological Sciences, University of Florida, Gainesville, FL, USA*

[2]*Securing Antarctica's Environmental Future, School of Earth, Atmosphere and Environment, Monash University, Clayton, Kulin Nations, Victoria, Australia.*

ABSTRACT.

Subglacial topography is critically important for simulating ice-sheet evolution and projecting sea-level contributions. However, the subglacial topography of the Antarctic ice-sheet is sparsely measured. Obtaining a gridded topography map used in ice-sheet simulations requires interpolating the measurements or inverting topography from observations of ice velocity and surface elevation. Traditional inverse methods based on the mass conservation law usually produce a single topography that is overly smooth and does not capture the non-uniqueness of the solutions to mass conservation. In this study, we develop a new method that combines geostatistical simulations with Markov chain Monte Carlo (MCMC) to stochastically generate different realizations of subglacial topography for regions with high ice velocity. This method uses a two-step approach that iteratively simulates large- and small-scale topography. We test this method on Denman and Totten glaciers. The final topography ensemble shows significant elevation differences from BedMachine and presents large topographic uncertainty. This topography ensemble can be incorporated into ensemble ice-sheet modeling, allowing for the propagation of topographic uncertainty into the uncertainty in sea level projections.

INTRODUCTION

Subglacial topography, the bed elevation beneath the ice, is a controlling factor in ice-sheet evolution. In coastal regions, the advance and retreat of grounding lines are associated with the slope, curvature, and elevation of the subglacial bed (Weertman, 1974; Schoof, 2007; Bradwell and others, 2019; Sergienko and Wingham, 2022). Thus, when modeling ice-sheet evolution, different estimates of subglacial topography can directly affect simulated ice-stream stability (Gasson and others, 2015; Wernecke and others, 2022; Castleman and others, 2022). Subglacial topography is also a critical component in multiple englacial and subglacial processes. For example, previous studies have demonstrated how subglacial topography influences basal traction (Bingham and others, 2017; Kyrke-Smith and others, 2018; Hoffman and others, 2022), geothermal heat flow (Colgan and others, 2021; Shackleton and others, 2023), ice deformation (Meyer and Creyts, 2017; Law and others, 2023; Liu and others, 2024), and subglacial hydrology (Siegert and others, 2016; MacKie and others, 2021b), each of which significantly impacts ice-sheet evolution, and hence the projected sea level rise contributions.

Despite its importance, Antarctic subglacial topography is only sparsely measured. Bed elevation measurements are primarily provided by airborne ice-penetrating radar, which samples data along the aircraft's flight lines. Densely sampled coastal regions of Antarctica have flight lines separated by five to twenty kilometers, and data gaps in inland Antarctica can easily exceed fifty kilometers (Frémand and others, 2023; Matsuoka and others, 2025).

These sparse bed elevation measurements must be interpolated to produce a gridded subglacial topographic map for ice-sheet modeling applications (e.g. Herzfeld and others, 1993). However, interpolated subglacial topography often violates physical constraints that are critical for ice-sheet models. Specifically, the estimated subglacial topography and resulting ice thickness must conserve ice mass. Seroussi and others (2011) showed that traditional interpolation methods, such as kriging, produce subglacial topography that violates the mass conservation constraint when integrated with observed ice velocity. This violation manifested as spurious, large-magnitude ice flux divergences, which can cause large and rapid changes in ice thickness in the first few time steps when simulating the glacier evolution.

To find a physically realistic subglacial topography producing realistic ice flow behaviors, several methods have been proposed to invert subglacial topography using physical models or constraints. These methods include numerically solving for subglacial topography from mass conservation (Morlighem and

others, 2011; McNabb and others, 2012), simultaneously inverting for subglacial topography and basal sliding parameters to reproduce observed ice velocity in ice flow models (e.g. Perego and others, 2014), inverting for subglacial topography that reproduces the observed surface elevation with a known surface climate forcing (van Pelt and others, 2013), and adopting machine learning approaches to find an optimal subglacial topography that minimizes ice flux divergences (Teisberg and others, 2021). These methods reconstructed subglacial topographies that show fewer physical artifacts when used with observed ice surface elevation or ice velocity, which is valuable for initiating ice flow models. Specifically, the method proposed in Morlighem and others (2011) has been used in BedMachine (Morlighem and others, 2017, 2020), a widely-used subglacial topography dataset, to estimate subglacial topography in the fast-flowing regions of the Antarctic and Greenland ice-sheets.

While the BedMachine estimate of subglacial topography in the fast-flowing region conserves ice mass, this solution to mass conservation has several limitations. First, the topography is often unrealistically smooth. Specifically, Morlighem and others (2011) used mass conservation to solve for an optimized subglacial topography that minimizes the gradients of ice thickness. This topography is not required to reproduce the topographic roughness in the bed elevation measurements (MacKie and others, 2021b) and is usually much smoother than the observed topography (Hoffman and others, 2022). Second, the subglacial topographic uncertainty is not robustly quantified and cannot be easily propagated into ice-sheet models. The topographic uncertainty in Morlighem and others (2011) is presented as a maximum error bound, which reflects how the errors in ice velocity, surface and basal mass balance, and surface elevation change rate might affect the optimized solution. However, this approach fails to account for subglacial topography solutions that do not minimize smoothness. In addition, the error bound does not represent each possible subglacial topography, and thus cannot be directly used to propagate topographic uncertainty into ice-sheet modeling results.

In contrast to deterministic interpolation approaches, geostatistical simulation methods can generate multiple realizations of subglacial topography with realistic morphology. Geostatistical simulations are methods that interpolate sparse measurements to produce a field of parameters (Deutsch and Journel, 1992; Goovaerts, 1997). Instead of creating a smooth topography interpolation that maximize accuracy, like with kriging, geostatistical simulation prioritizes reproducing the spatial variability, or roughness, of the topography (Goff and others, 2014; MacKie and others, 2020; Neven and others, 2021). In addition, geostatistical simulation stochastically generates multiple equally probable realizations of the topography,

which quantifies uncertainty arising from sparse measurements and allows propagting this uncertainty into glacier models (e.g. Wernecke and others, 2022).

Subglacial topography generated by geostatistical simulation has supported scientific discoveries about glacier systems. For example, Zuo and others (2020) and MacKie and others (2021a) used geostatistically simulated topography to show that subglacial water routing paths are highly sensitive to topographic uncertainty. In thermodynamic modeling of ice deformation, Law and others (2023) found that using geostatistically simulated topography led to enhanced ice deformation and a variable-thickness temperate ice layer at the base, which aligned more closely with borehole temperature observations. In contrast, the model with the BedMachine topography produced reduced ice deformation and a thin basal temperate ice layer.

Although traditional geostatistical simulation methods can preserve topographic roughness and quantify uncertainty due to sparse measurements, they do not conserve mass and can consequently introduce physical inconsistencies in ice flux. As a first step in addressing the issue, MacKie and others (2021b) employed a co-simulation technique in which topography is geostatistically simulated to correlate with mass-conserving topography from BedMachine (Morlighem and others, 2017). Although this approach visually aligned topographic realizations more closely with mass conservation constraints, it did not guarantee that ice mass is conserved, as the mass conservation equation is neither explicitly used nor proven to be satisfied in the workflow.

To reconcile the needs of imposing the mass conservation constraint, preserving realistic roughness, and estimating topographic uncertainty, we integrate geostatistical simulation with mass conservation enforcement to generate subglacial topography realizations. This integration allows geophysical inversion to recover topography that remains realistically rough. Geostatistical inversion has previously been applied in other disciplines, such as petroleum exploration and groundwater hydrology. Geostatistical inversion is typically implemented in a Markov chain Monte Carlo (MCMC) framework, where random subsets of the parameter field are iteratively geostatistically perturbed until a geophysical forward model agrees with observations (Fu and Gómez-Hernández, 2008; Mariethoz and others, 2010; Nunes and others, 2012; Shamsipour and others, 2010; Volkova and Merkulov, 2019; Reuschen and others, 2020). In this framework, geostatistical realizations are repeatedly updated and tested against physical constraints, which produces stochastic samples that preserve spatial structure while satisfying governing equations (e.g. Hansen and others, 2012). Once convergence is achieved, additional samples are drawn to form an ensemble that

quantifies uncertainty. This strategy is advantageous because it explores the parameter space without requiring a closed-form solution to the inverse problem, making it well-suited for non-unique problems. In this paper, we adopt a similar MCMC approach where subglacial topography is iteratively updated using geostatistical methods, and the update is accepted or rejected based on mass conservation criteria.

In what follows, we first describe the study regions, observational data used, and the quality control of bed elevation data. Next, in the Methods section, we outline the workflow, review the key theories, and explore the implementation details. In the Results section, we quantitatively present the subglacial topography realizations sampled by the geostatistical MCMC. Finally, in the Discussion section, we discuss the implications of the results and future applications.

STUDY REGIONS AND DATA

Study Regions

We apply our method to the Denman Glacier and Totten Glacier regions where ice velocity exceeds 50 $m\ a^{-1}$. Denman and Totten Glaciers are major outlet glaciers in East Antarctica with an annual ice discharge of ∼59.2 Gt and ∼71.4 Gt from 2009 to 2017, respectively (Rignot and others, 2019). Denman Glacier is thought to rest on a steep retrograde bed slope near its current grounding line, making it vulnerable to rapid future retreat (Morlighem and others, 2020). Specifically, BedMachine estimates the subglacial topography beneath Denman Glacier to be as deep as 3500 meters below sea level (Morlighem and others, 2020). However, the shape and depth of the trough are not well-resolved in ice-penetrating radar, where the radar measurements at the center of the trough do not capture clear return signals from the bed (Liu and others, 2016; MacGregor and others, 2021). These potentially erroneous bed elevation measurements of the trough present challenges for inverting for subglacial topography. The second study region, Totten Glacier, is characterized by a large area of high-velocity ice and relatively smooth topography. Widespread grounding line retreat has been observed over Totten Glacier (Aitken and others, 2016) with large basal hydrology channels that could affect the glacier's evolution (Dow and others, 2020; Pelle and others, 2024). These two case studies represent subglacial environments with different characteristics, providing diverse test cases for our method.

Data Sources

The data used to reconstruct the subglacial topography are presented in Fig. 2 and Fig. 3. We use MEaSUREs InSAR-Based Antarctica Ice Velocity Map version 2 (Rignot and others, 2017) for ice surface velocity, which is available at 450 m resolution (Fig. 2b, Fig. 3b). We use ice surface elevation in BedMachine v3 at 500 m resolution (Morlighem and others, 2020), which is inferred from the Reference Elevation Model of Antarctica dataset (Howat and others, 2019) with firn-depth corrections (Fig. 2b, Fig. 3b). To distinguish between surface topography and subglacial topography, we only refer to surface topography as surface elevation in the following sections. We obtain the classification of regions (grounded ice/floating ice/open ocean/ice-free) from BedMachine at 500 m resolution (Fig. 2c, Fig. 3c). We obtain the surface elevation change rate by averaging the elevation change between May 2014 and May 2016 from MEaSUREs ITS_LIVE Antarctic Grounded ice-sheet Elevation Change version 1 at 1.92 km resolution (Nilsson and others, 2023) (Fig. 2d, Fig. 3d). We also obtain the surface mass balance by averaging the surface mass balance between 2014 and 2016 estimated by Regional Atmospheric Climate MOdel (RACMO2.3p2), which outputs at 27 km resolution (van Wessem and others, 2018) (Fig. 2e, Fig. 3e). We fit all data listed above onto a regular grid with 1 km resolution, which is also the grid used for simulating subglacial topography. We use nearest neighbor interpolation for classification of regions, and linear interpolation for all other data.

We compile bed elevation measurements on a 1 km resolution regular grid in polar stereographic coordinate using multiple datasets (Fig. 2a, Fig. 3a). In the grounded ice region, we use bed picks from ice-penetrating radar data assembled in Bedmap2 (Fretwell and others, 2013) and Bedmap3 (Frémand and others, 2023). Each grid cell in the grounded ice region is assigned the average bed elevation from the available radar measurements within that cell. If no measurements are available, the cell remains empty. In the following sections, the grid cells assigned with values are referred to as bed elevation measurements. Several radar campaigns are used in the study region: the NASA Operation IceBridge campaign (MacGregor and others, 2021), the ICECAP campaign (Young and others, 2011; Blankenship and others, 2017), the ICECAP-EAGLE campaign (Young and others, 2016; Roberts and others, 2023), the ICECAP-OLDICE campaign (Young and others, 2016), the Talos-Dome campaign in 2003 (Bianchi and others, 2003), and the Stanford-Cambridge Radar Film Digitization Project (Schroeder and others, 2019).

For regions classified as ice-free ocean, floating ice, and ice-free land, we project the BedMachine v3 bed elevation (Morlighem and others, 2020) from its 500 m grid to our 1 km grid using linear interpola-

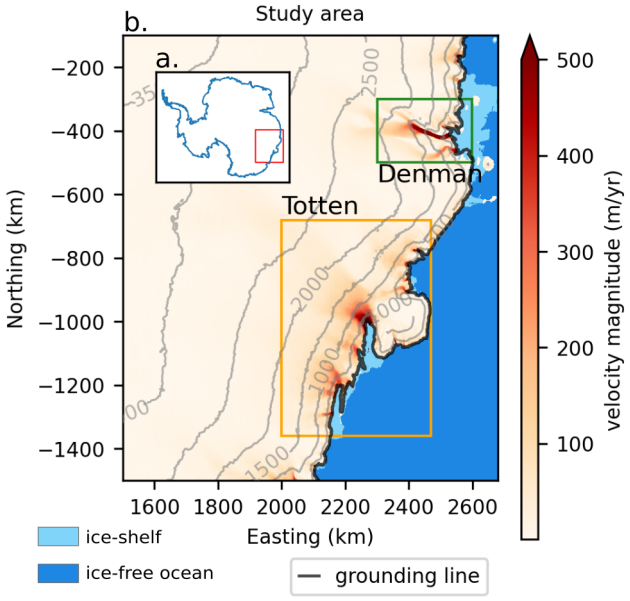

Fig. 1. (a) Antarctic ice-sheet grounding lines (solid black lines) (Haran and others, 2018) and the zoom-in region in East Antarctica shown in subplot b. (b) Ice surface velocity magnitude (Rignot and others, 2017) overlaid by contour lines of the surface elevations (Howat and others, 2019) with ice shelf and open ocean region colored as light and deep blue, respectively (Morlighem and others, 2020)

tion. Bedmap2 and Bedmap3 data are converted from EIGEN-GL04C geoid (Foerste and others, 2005) to EIGEN-6C4 geoid (Foerste and others, 2014) used in BedMachine to ensure consistency between different datasets.

Data Quality Control

We perform quality control on bed elevation data to identify and remove potentially erroneous measurements. Bed elevation measurements could be affected by instrumental errors, radio-wave velocity errors, bed-picking errors, GPS errors, and clutter (Lapazaran and others, 2016). Clutter occurs when radar echoes are reflected from off-nadir topographic high points, which often happens on high-relief subglacial topography such as deep troughs. Compared to other sources of positive or negative errors, radar clutter can cause the returned bed elevation to have a large-magnitude positive bias (Lapazaran and others, 2016; Scanlan and others, 2020).

Radar errors complicate bed mapping efforts. Often, the quality control of bed elevation data is performed by visual inspection or by comparison with other data sources at a few cross-over locations (e.g. Farinotti and others, 2014; Lippl and others, 2020), which lacks a quantitative assessment. In this paper, we implement an MCMC quality control procedure. We first exclude bed elevation measurements that are

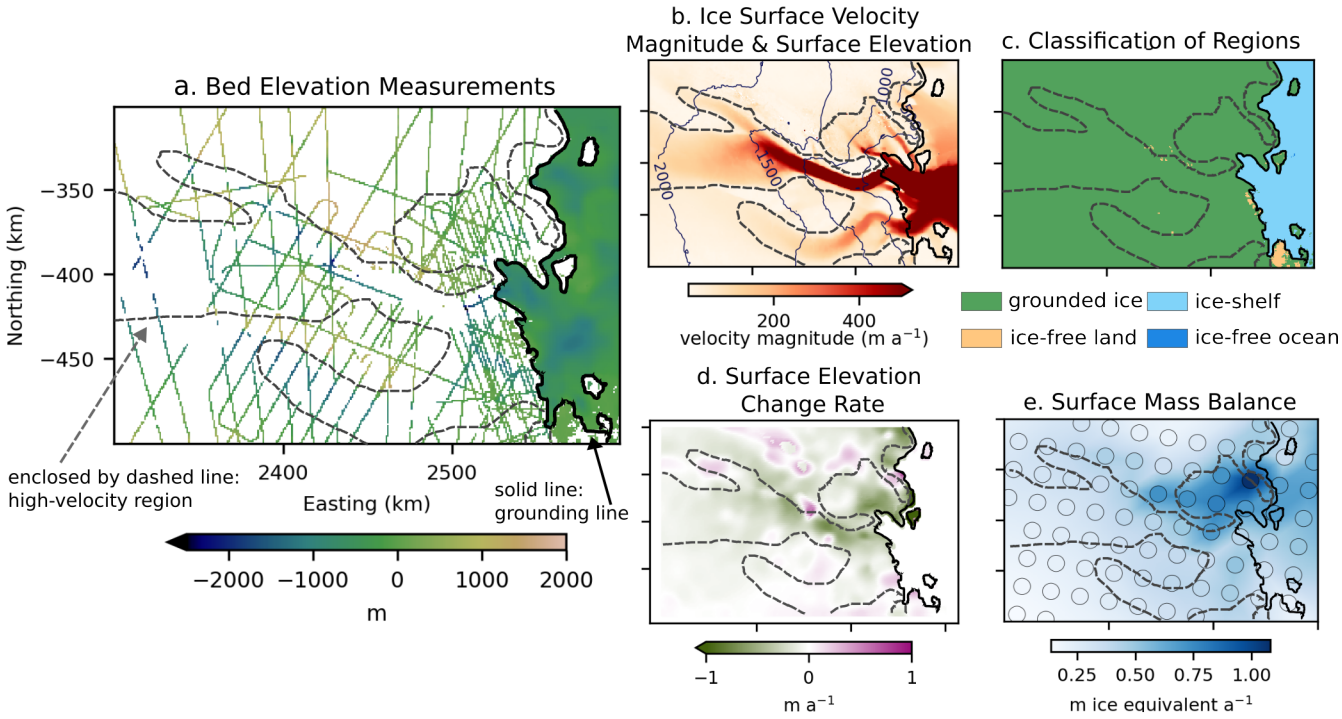

Fig. 2. Processed datasets used for inverting for subglacial topography at Denman Glacier. The dashed gray line delineates regions with ice surface velocity magnitude greater than 50 m/yr. The solid black line represents grounding lines traced based on BedMachine region classification (Morlighem and others, 2020). Subplot a shows gridded bed elevation measurements in Denman Glacier before the quality control step (Fretwell and others, 2013; Frémand and others, 2023; Morlighem and others, 2020), where ice-free land, ice-shelf, and ice-free ocean regions have BedMachine subglacial topography / bathymetry. Subplot b plots ice surface velocity magnitude (Rignot and others, 2017) overlaid by the contour lines of the surface elevation (Morlighem and others, 2020; Howat and others, 2019); c shows the classification of regions obtained from BedMachine (Morlighem and others, 2020); d shows surface elevation change rate (Nilsson and others, 2023); e shows the interpolated surface mass balance overlaid by the original surface mass balance estimations (van Wessem and others, 2018) marked in black-edge circles.

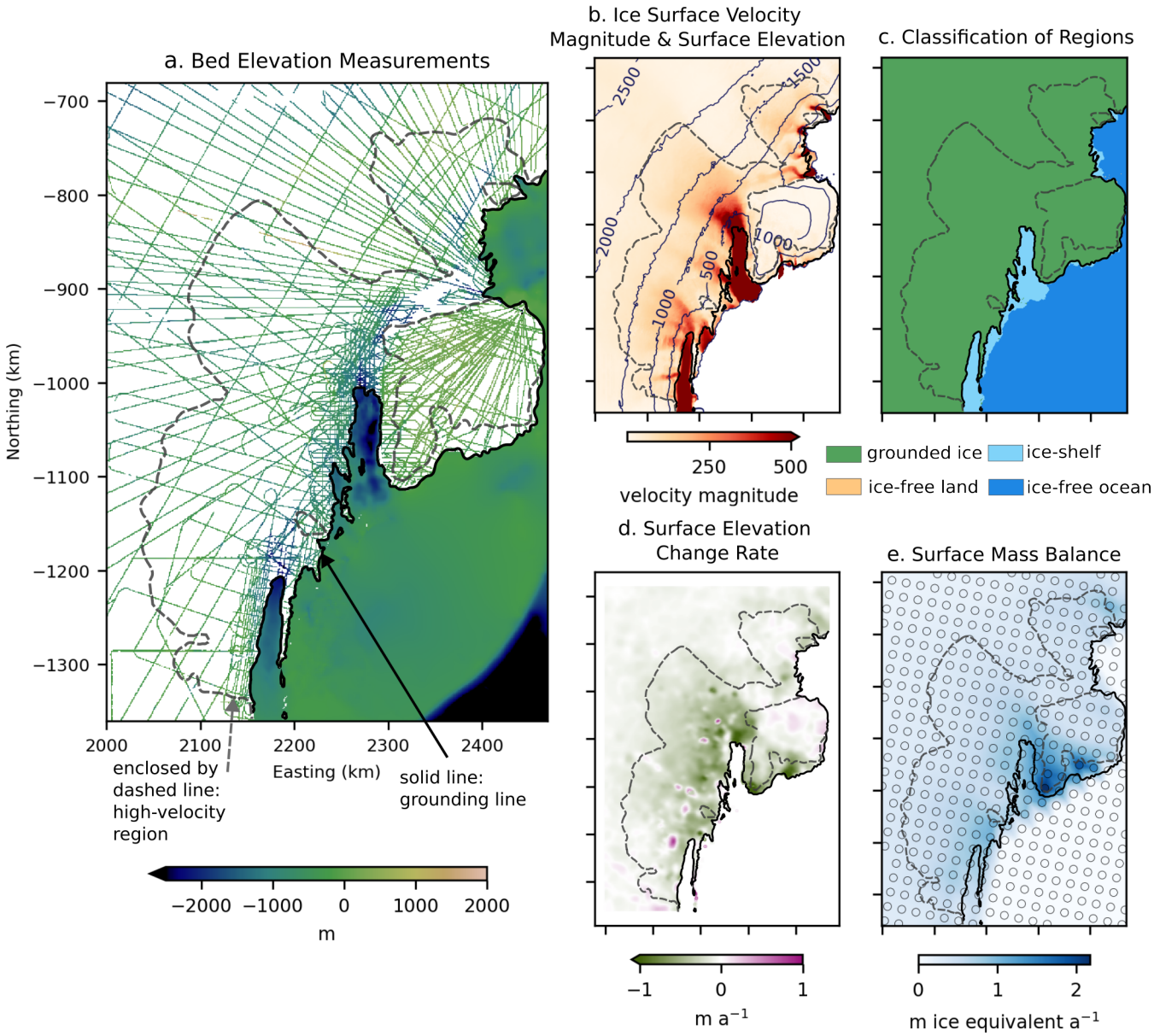

Fig. 3. Processed dataset used for inverting subglacial topography of Totten Glacier, similar to Fig. 2. The dashed gray line delineates regions with ice surface velocity magnitude greater than 50 m/yr. The solid black line represents grounding lines traced based on BedMachine region classification (Morlighem and others, 2020). Subplot a shows gridded bed elevation measurements before the quality control step (Fretwell and others, 2013; Frémand and others, 2023; Morlighem and others, 2020), where ice-free land, ice-shelf, and ice-free ocean regions are colored by BedMachine subglacial topography / bathymetry. Subplot b plots ice surface velocity magnitude (Rignot and others, 2017) overlaid by contour lines of the surface elevation (Howat and others, 2019); c shows the classification of regions obtained from BedMachine (Morlighem and others, 2020); d shows surface elevation change rate (Nilsson and others, 2023); e shows interpolated surface mass balance map overlaid by the original surface mass balance estimations (van Wessem and others, 2018) marked in black-edge circles.

greater than or equal to ice surface elevation. Then, we perform a Metropolis-Hasting MCMC analysis (Metropolis and others, 1953; Hastings, 1970), which perturbs the subglacial topography using spatially-correlated noise and accepts or rejects realizations based on penalties for ice flux divergences and misfits from bed elevation measurements. This analysis provides subglacial topography realizations that reduce spurious ice flux divergences while maintaining differences to bed elevation measurements comparable to those in BedMachine, allowing us to identify and exclude measurements that cannot be reconciled with a mass-conserving topography. To address the potential large-magnitude radar errors, potentially from radar clutter and other erroneous measurements, we remove bed elevation measurements that are 1.5 standard deviations shallower than the generated subglacial topography realizations. The full details of the data quality control step are documented in the Supplementary Material Section 1, 2.

For the Denman region, we also remove 10 additional grid cells on a radar flight line near the narrowed trunk of the glacier, where a subglacial trough likely exists and could potentially cause significant bed elevation errors (Forte and others, 2019). For the Totten region, we remove additional bed elevation measurements from one radar flight line, which have at least 1000 m cross-over absolute errors with data from multiple other radar flight lines. These additional bed elevation measurements removed also are not used in BedMachine topography (Morlighem and others, 2020).

In total, we removed 1.45% and 2.2% of bed elevation measurements in Denman's and Totten's regions of high-velocity ice, respectively. For context, we compared the removed bed elevation measurements to BedMachine (Morlighem and others, 2020) and BedMap gridded subglacial topography (Pritchard and others, 2025). For Denman Glacier, the average absolute difference with BedMachine is 2356 m, while the difference with Bedmap is 1829 m. For Totten Glacier, the same comparisons yield differences of 667 m and 595 m, respectively.

METHODS

Overview

We present an MCMC approach to generating subglacial topography realizations in regions with high-velocity ice, such that the realizations conserve ice mass, honor bed elevation measurements, and have realistic roughness. The MCMC algorithm iteratively proposes new topography and evaluates the proposed topography by mass conservation. We design two steps to generate topography realizations, where each step constructs Markov chains with a distinct proposal method and creates topographic features of different

spatial scales (Fig. 4). In the first step, we generate large-scale topographic features (lateral dimension > 10 km) that improve the consistency with mass conservation (Fig. 4a). We run Markov chains, which we refer to as large-scale chains, that iteratively propose new topography by adding blocks of perturbations to the previous topography. These large-scale chains generate subglacial topographies that preserve the bed elevation measurements, but they do not guarantee realistic topographic roughness. In the second step, we update topography sampled from large-scale chains to honor the spatial roughness of subglacial topography (Fig. 4b). In this step, we run a second set of Markov chains, which we refer to as small-scale chains, that propose new topography by replacing small-scale features (lateral dimension $\leqslant$ 10 km). These new features are generated by Sequential Gaussian Simulation, a geostatistical interpolation method that honors the spatial roughness of the simulated topography. The final topography ensemble consists of the topography produced in each small-scale chain, which capture diverse topographic features with realistic roughness while maintaining low mass conservation misfits.

In the following subsections, we first summarize key concepts in geostatistics, mass conservation, and MCMC to discuss how they are adapted for simulating subglacial topography. Then we describe the implementation details of the large-scale chain and small-scale chains. At the end, we outline how these chains are combined to generate the topography ensemble.

Geostatistics: the bed elevation constraint

Observations of subglacial topography provide direct elevation constraints and information on spatial correlation of topographic features. The latter is visually expressed as the topography's roughness and can be quantified by semi-variogram statistics (e.g. MacKie and others, 2021b). The semi-variogram, often referred to simply as the variogram, summarizes the spatial statistics observed in the sparse bed elevation measurements. It describes the two-point correlation structure by relating the lag distance (separation distance) between two elevation measurements to their value differences (Zimmermann and others, 2008):

$$\gamma(h) = \frac{1}{2N(h)} \sum_{i=1}^{N(h)} (T(x_i) - T(x_i + h))^2. \tag{1}$$

In Equation 1, h is the lag distance. $T(x_i)$ is the bed elevation at the location x_i. $x_i + h$ represent locations that are h away from x_i. $N(h)$ is the num.ber of data pairs separated by distance h. Intuitively, when two grid cells on the topography map are farther away (a larger h), their elevations are less correlated (a larger $\gamma(h)$) until they are far enough apart that the correlation vanishes ($\gamma(h)$ reaches a plateau),

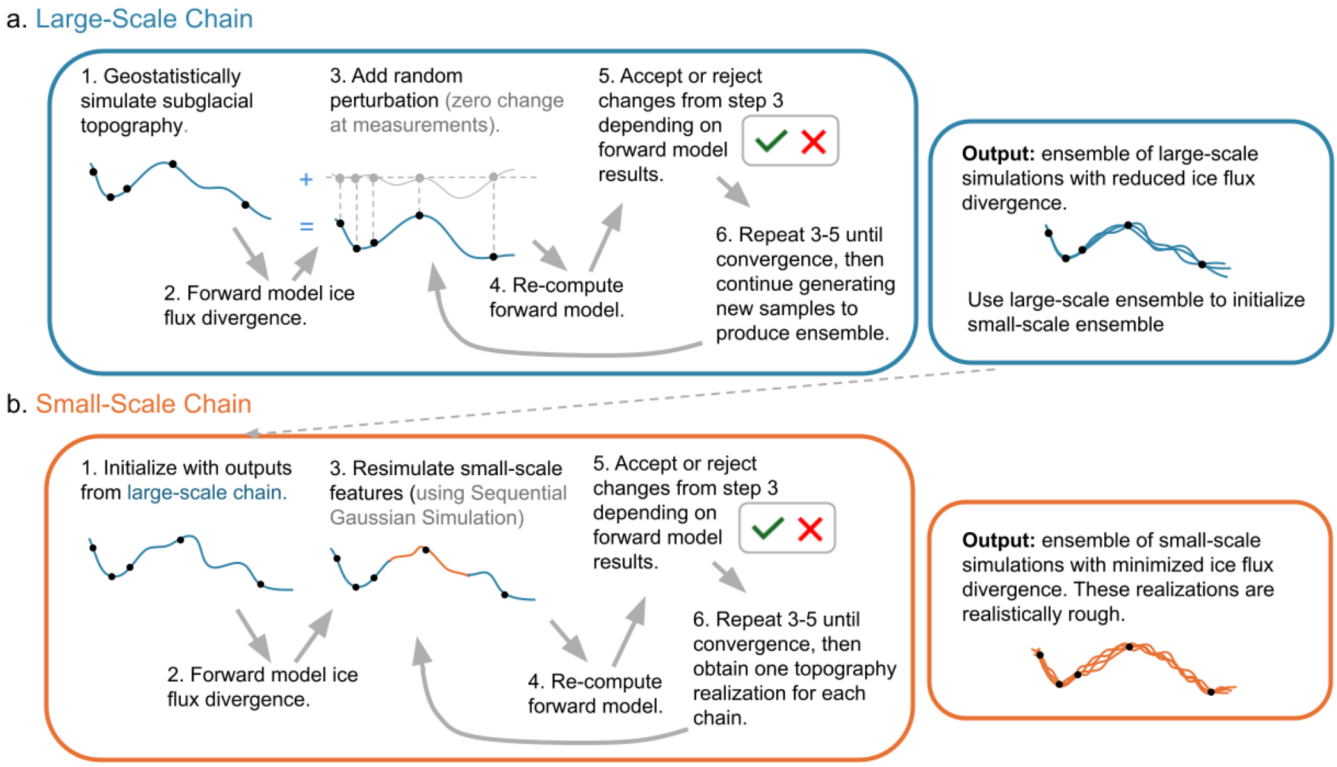

Fig. 4. A simplified schematic diagram for using the large-scale and small-scale chains to generate subglacial topographies. We present subglacial topographies as 1D lines for simplification. Subplot a represents the large-scale chains, where new subglacial topography (blue lines) are proposed by adding random perturbations (gray line in step 3). Subplot b represent the small-scale chains, where the small-scale features in the topography are replaced by simulations generated by SGS (orange lines).

leading to a typical variogram shape where $\gamma(h)$ increases with h until reaching a plateau. The empirical variogram calculated from sparse measurements can be fitted into a variogram model, defined by the variogram model type (Gaussian, Spherical, Exponential, or Matern). The variogram model is described by the range (maximum $\gamma(h)$), sill (h at which $\gamma(h)$ reaches maximum), and nugget ($\gamma(0)$) parameters. A smaller range or a larger sill could indicate large variability of subglacial topography over a short spatial distance, and vice versa. The variogram model can be used for comparing the spatial roughness of different subglacial topographies and for generating topography with realistic roughness (MacKie and others, 2021b). In this paper, we use functions in SciKit-Gstats Python package with the Cressie estimator to compute experimental variograms and fit variogram models (Mälicke, 2022).

While kriging interpolation uses the variogram to provide a single deterministic estimate of the bed, Sequential Gaussian Simulation (SGS) generates multiple realizations of subglacial topography that honor sparse bed elevation measurements while reproducing the variogram statistics (MacKie and others, 2021b). SGS is a geostatistical conditional simulation method that stochastically interpolates sparse measurements to produce equally probable realizations of a random field. SGS is a 'conditional' simulation method because the generated realizations exactly match available measurements. SGS has been shown to be effective in stochastically generating subglacial topography in regions with slow ice flow (e.g. MacKie and others, 2020; Law and others, 2023); but when it is used for regions with fast ice flow, the simulated subglacial topography is often incompatible with mass conservation. Additionally, in some regions with high-relief topographic features, incomplete radar sampling may limit the range of bed elevations represented in SGS realizations. For example, in the Denman region, BedMachine (Morlighem and others, 2020) and Bedmap3 (Pritchard and others, 2025) resolve a deep subglacial trough reaching elevations of -3700 m and -2800 m respectively, whereas the bed elevation measurements within 50 km of the trough only reach -2200 m. In cases where the true bed elevation in large data gaps differs greatly from the surrounding topography, the Gaussian nature of SGS makes its realizations unlikely to reproduce prominent features with elevations that extend beyond the range of measurements (Fig. S4). This limitation means that SGS alone is insufficient for sampling subglacial topography in regions with extreme relief.

To address this limitation, we adapt geostatistical simulation for mass-conserving topographies by dividing the process into two stages: (1) generating the large topographic features in the large-scale chains, and (2) re-simulating finer features constrained by the variogram statistics in the small-scale chains. We use SGS implemented in MacKie and others (2023) to generate topography in regions with low-velocity ice,

to initiate the large-scale chains, and to simulate realistically rough topographies in the small-scale chains.

Mass conservation: the physical constraint

Mass conservation provides valuable information to ensure the compatibility of simulated topographies with other ice surface observations, such as ice surface velocity, surface mass balance, and surface elevation change rate (Seroussi and others, 2011). The mass conservation equation (2) is derived by depth-integrating the ice continuity equation under the assumption of incompressible ice. The equation relates the sparsely measured subglacial topography with high-resolution ice velocity.

$$\frac{\partial H}{\partial t} = -\nabla \cdot (\bar{u}H) + \dot{M}_s + \dot{M}_b. \tag{2}$$

Here, $\frac{\partial H}{\partial t}$ is the rate of change of ice thickness; $\nabla \cdot (\bar{u}H)$ is the depth-integrated ice flux divergence, which calculates the volume of ice entering and leaving an ice column of thickness, H, with depth-averaged velocity, $\bar{u}$. Surface processes, such as surface accumulation (positive) and surface ablation (negative), are represented by the surface mass balance, $\dot{M}_s$; whereas the basal mass balance, $\dot{M}_b$, includes basal accumulation (positive) and basal ablation (negative).

We make further adjustments to adapt this universal equation to the available data in the study region. The ice thickness is expressed as the difference between ice surface elevation (S) and bed elevation (T). The annual change in bed elevation is usually orders of magnitude smaller than the change in surface elevation; therefore, we assume $\frac{\partial H}{\partial t} = \frac{\partial (S-T)}{\partial t} \approx \frac{\partial S}{\partial t}$. As annual basal mass balance is estimated to be in centimeter-scale or smaller in the grounded ice region (e.g., Seroussi and others, 2019; McArthur and others, 2023), we approximate $\dot{M}_b$ as 0. Additionally, the depth-averaged velocity, $\bar{u}$, is approximated by surface velocity, u_s, which is a reasonable assumption in the high-velocity regions where basal sliding dominates (Seroussi and others, 2011; Rignot and others, 2011).

Since mass conservation is most effective in high-velocity regions, we first define an inversion domain where our method can be applied. Assuming $u_s \approx \bar{u}$, we identify grounded ice regions with surface velocities greater than or equal to 50 m a^{-1}. We compute a mask of the region, smooth its boundary using a 15-cell mode filter, and then expand the mask outward by 3 km. Grid cells classified as open ocean, floating ice, and ice-free land are excluded from the region. This region (shown in Fig. 2 and Fig. 3), referred to hereafter as the high-velocity region, defines the domain where we apply the MCMC algorithm. Outside the high-velocity region, topography realizations are generated directly using SGS (e.g. MacKie and others,

2023).

After the adjustments, the mass flux residuals, which represent the ice flux divergence unresolved in the mass conservation equation, are defined as:

$$r = \nabla \cdot (u_s(S - T)) + \frac{\partial S}{\partial t} - \dot{M}_s. \tag{3}$$

The mass flux residuals are calculated for each grid cell in the high-velocity region. Spatial derivatives, such as ∇, are computed using second-order central differences. For simplicity, the spatial discretization notation to represent r at each grid cell (i, j) (e.g. r_{ij}) is omitted in this and following equations, similarly for S, T, $\frac{\delta S}{\delta t}$, and $\dot{M}_s$.

Bayes' theorem and MCMC: combining bed elevation measurements and mass conservation

Mass conservation provides a powerful physical constraint on subglacial topography, but by itself it cannot uniquely resolve the topography. To overcome this limitation, we combine mass conservation with bed elevation measurements in a Bayesian framework. Bayes' theorem offers a convenient framework to integrate these complementary sources of information into a posterior distribution of subglacial topography. Bed elevation measurements, such as the measured values and topographic roughness, define the prior distribution, $p(T)$. The spurious ice fluxes due to violations of mass conservation describe the likelihood function of the subglacial topography, $p(d|T)$, where d contains $[S, u_s, \frac{\delta S}{\delta t}, \dot{M}_s]$. Combining the prior and likelihood yields the posterior distribution of subglacial topography according to Bayes' theorem:

$$p(T|d) = \frac{p(d|T)p(T)}{p(d)}. \tag{4}$$

Because the posterior distribution defined by Bayes' theorem cannot be obtained analytically, we use Markov chain Monte Carlo (MCMC) to approximate it. MCMC is a well-established sampling method that generating a sequence of samples (a Markov chain) from complex distributions (Gallagher and others, 2009; Geyer, 2011). At each iteration, MCMC proposes a perturbation to the current realization of the parameter field, creating a new candidate. This new candidate is then evaluated against the prior and the physical constraint using the likelihood function. This evaluation determines whether the new candidate is accepted or rejected. Typically, the chain run for many iterations until convergence, after which subsequent

realizations are used to approximate the posterior. In our application, the Markov chain is composed of a sequence of subglacial topography realizations T_i with $i \in 0, 1, 2, 3....$

There are many different MCMC sampling algorithms. We use the widely used Metropolis-Hastings (MH) approach (Metropolis and others, 1953; Hastings, 1970), which efficiently balances optimization with exploration of the parameter space and is known for its simple and flexible implementation. In this framework, candidate topographies with lower misfit (i.e., lower mass flux residuals) are usually accepted, while those with higher misfit can still be accepted with some probability. This strategy prevents the chain from becoming trapped in local solutions, enabling the exploration of plausible subglacial topographies. Starting from an initial guess of subglacial topography T_0, each T_i is iteratively generated i as described below.

1. propose a new realization T' by updating T_i
   denote the probability of obtaining T' from T_i as $q(T'|T_i)$
2. compute posterior distribution of T': $p(T'|d) = \frac{p(d|T')p(T')}{p(d)}$
   compute posterior distribution of T_i: $p(T_i|d) = \frac{p(d|T_i)p(T_i)}{p(d)}$
3. compute acceptance probability $\alpha(T', T_i) = \min\left[\frac{p(d|T')p(T')q(T_i|T')}{p(d|T_i)p(T_i)q(T'|T_i)}, 1\right]$
4. with probability $\alpha(T', T_i)$, accept T' and let T_{i+1} be T'
   with probability $1 - \alpha(T', T_i)$, let T_{i+1} be T_i

The proposal step in the MCMC algorithm searches through the space of possible subglacial topographies, while the acceptance probability α governs which candidate topography samples are retained.

In our method, we adopt a special case of the Metropolis-Hasting algorithm, called Extended Metropolis algorithm (Mosegaard and Tarantola, 1995). The key difference is that, rather than explicitly evaluating the prior $p(T)$, Extended Metropolis directly generates proposed topography from the prior distribution. In other words, the proposal distribution equilibrates to the prior distribution such that

$$\frac{q(T_i|T')}{q(T'|T_i)} = \frac{p(T_i)}{p(T')}, \tag{5}$$

and the acceptance probability is simplified to a comparison of likelihoods:

$$\alpha(T', T_i) = \min\left[\frac{p(d|T')}{p(d|T_i)}, 1\right]. \tag{6}$$

The Extended Metropolis algorithm is particularly well-suited to our problem because the prior distribution of subglacial topography can be efficiently represented by geostatistical simulations. In this framework, candidate realizations are drawn directly from the geostatistical prior, which ensures that the proposals already satisfy the geostatistical properties of the bed while the acceptance step enforces consistency with mass conservation. A similar approach was applied in Hansen and others (2012), where geostatistical priors were used to generate proposals directly from simulation. We utilize different proposal methods in the large-scale chain and the small-scale chain to update the topography, and we explain their associated priors in the later sections. The likelihood function is represented by $p(d|T)$, where d contains $S, u_s, \frac{\delta S}{\delta t}, \dot{M}_s$. We define $p(d|T)$ in terms of the spurious mass flux residuals r for a given topography T.

Ideally, the mass flux residuals r should be zero upon convergence, but in practice, uncertainties in ice velocity, surface mass balance, and surface elevation change rate introduce nonzero values of r. To account for these potential uncertainties, we define r at every grid cell to be an independent Gaussian distribution with standard deviation, σ_r, as shown below.

$$p(d|T) = \exp\left(-\frac{\sum(r^2)}{2\sigma_r^2}\right). \tag{7}$$

We use BedMachine as a baseline mass-conserving topography to calibrate σ_r and test our method's ability to reduce mass flux residuals. Specifically, we approximate the distribution of r by fitting a Gaussian distribution to the mass flux residuals from the BedMachine topography in the high-velocity region, yielding $\sigma_r \approx 3.5\ m\ a^{-1}$ at Denman Glacier and $\sigma_r \approx 4.5\ m\ a^{-1}$ at Totten Glacier. While this calibration is not fully independent–since BedMachine is also used as a benchmark–we note that σ_r functions primarily as a scaling parameter in the likelihood. Its role is to control how strongly mass flux residuals are penalized, rather than to bias inference towards BedMachine, and our results are not sensitive to modest changes in its value. In Supplementary Material Section 3, we further evaluate r in regions with dense subglacial measurements to confirm that the Gaussian distribution estimated from BedMachine falls within the plausible range of residual values. Ideally, σ_r would be derived from uncertainties in ice velocity, surface mass balance, and surface elevation change rate, but in practice this would be difficult to implement consistently. Other possible approaches for defining the distribution of mass flux residuals based on data uncertainties are discussed in the Discussion section.

Large-scale chain: reconstruct large geometries

As discussed in the Geostatistics section, the Gaussian nature of SGS means that SGS may overlook large features such as deep troughs. As such, we use a two-step MCMC geostatistical inversion procedure that resolves both the large- and small-scale features (Fig. 4). In the first step, we construct Markov chains to resolve large-scale subglacial topographic features (lateral dimensions > 10 km) that reduce the mass flux residuals.

The large-scale chains search for topographies that satisfy both mass conservation and direct bed elevation measurements, without imposing restrictions on topographic roughness. We start each large-scale chain with an initial guess of the subglacial topography individually generated by SGS (Fig. 4a, step 1). Then we iteratively perturb the topography (Fig. 4a, step 3) by adding blocks of Weighted Random Fields (WRF). WRFs are spatially correlated random fields set to zero at the locations of bed elevation measurements, which ensures that observations are preserved while allowing smooth perturbations elsewhere. Because roughness is not enforced, this prior is relatively uninformative, which enables MCMC to capture high-relief features such as troughs when required to conserve mass. We improve convergence by perturbing only one block of topography per iteration (e.g. Roberts and Sahu, 2002). Updating the entire domain often results in favorable changes in one region being canceled by unfavorable changes in others, which lowers acceptance rates. In contrast, block-based updates effectively increases acceptance rates and accelerates convergence. The blocks selected throughout the MCMC algorithm could repeat and overlap, and the subglacial topography at each grid cell is perturbed more than once.

The block perturbation process is illustrated in Figure 5. At each iteration, a random block is chosen within the high-velocity region (Fig. 5, step 3.1), with lateral dimensions drawn from a uniform distribution between 20 and 100 km for Denman Glacier and between 50 and 200 km for Totten Glacier. These block sizes ensure the acceptance rates to remain between 0.1 and 0.4, which usually indicates an efficient MCMC algorithm (Geyer, 2011; Gelman and others, 1997). Second, a random field with the same size as the block is generated (Fig. 5, step 3.2). The random field is sampled from a multivariate Gaussian distribution with zero mean and an exponential, isotropic covariance model, which allows us to efficiently generate the field using Fourier Transforms implemented in the Python package GSTools (Müller and others, 2022). This covariance model can be represented by a variogram with zero nugget and a range sampled uniformly between 10 and 45 km for the study of Denman Glacier. The maximum range (45 km) represents the variogram range calculated from bed elevation measurements inside the high-velocity region of Denman

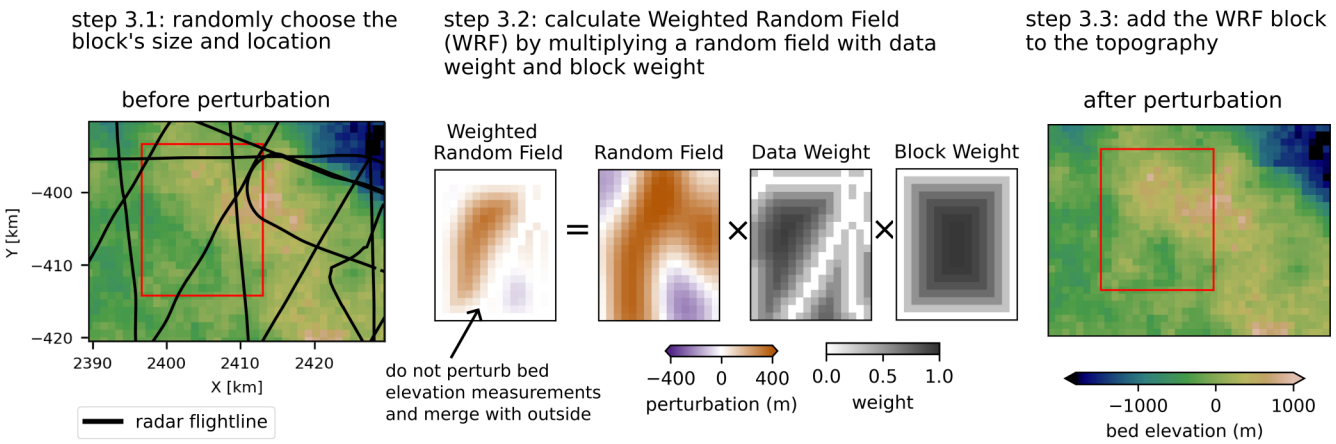

Fig. 5. The figure expands on the step 3 in Fig. 4a to illustrates the proposal method used in the large-scale chain. The red rectangle in step 3.1 and step 3.3 represent the selected random block.

Glacier, and the minimum range helps to create perturbations that resemble relatively smaller topographic features. With a similar process, the covariance model is chosen to be between 10 and 80 km for Totten Glacier. The amplitude of the random field is sampled from a uniform distribution between 50 and 200 m for Denman and between 100 and 300 m for Totten, which we tuned to keep acceptance rates between 0.1 and 0.4. We then multiply the random field with the weight matrices to force values to taper smoothly to zero at locations with bed elevation measurements and blocks edges (Fig. 5, step 3.2; also see Supplementary Material Section 4). Finally, we add the WRF to the topography inside the block (Fig. 5, step 3.3). Outside the high-velocity region, the topography is masked out and remains unchanged.

Like other MCMC applications, our method requires an initialization period, or burn-in, during which the chain iteratively updates the initial guess before reaching a stationary distribution (i.e., iterations after which the topography realizations are mass conserving). Thus, we discard the early iterations where the large-scale features have not yet converged to a stationary distribution. We use a trace plot (Fig. S3) to determine how many iterations to discard (Supplementary Material Section 5).

The subglacial topography samples generated in the large-scale chain after burn-in are used to find the topographic trend and serve as initial guesses for the small-scale chains. After the burn-in phase, We first calculate the topographic trend, T_{trend}, by taking a topography sample from each large-scale chain and applying a Gaussian smoothing filter with a standard deviation of 5 km. Then we sample 10 topography realizations from each of the 4 large-scale chains to initialize the small-scale chains. Because consecutive iterations in a Markov chain are correlated, we only sample at every k-th iteration to ensure approximate independency between sampled subglacial topographies. This method, called thinning in

MCMC literature, is often used to reduce autocorrelation between samples (Jones and Qin, 2022). The value of k is determined by calculating the autocorrelation of topography across iterations (Fig. S4), which is 4000 iterations for Denman Glacier and 30000 iterations for Totten Glacier (e.g. Mosegaard and Tarantola, 1995). Together, each large-scale chain provides a T_{trend} and 10 realizations, $T_{samples}$, which are used to initialize 10 small-scale chains.

Small-scale chain: simulate finer features

Following the large-scale chain, the small-scale chain uses SGS to re-simulate small-scale features (lateral dimension $\leqslant$ 10 km) that are not captured by the large-scale trend. Similar to Hansen and others (2012), each proposal consists of simulating a sub-region of the topography with SGS (Fig. 4b; Fig. 6). In this way, small-scale features in the initial topography is iteratively replaced with SGS-generated realizations, which preserves realistic roughness. The SGS proposes updates that are constrained by both bed elevation measurements and topographic roughness, enforcing a geostatistical prior on the subglacial topography. Because these updates are still subjected to the MCMC acceptance criterion, the simulated features remain constrained by the likelihood from mass conservation, as in the large-scale chains.

We initialize the small-scale chains with the topographic trend obtained from the large-scale chain. We first remove large topographic features by subtracting T_{trend} from T_{sample} (a.k.a. de-trending). Then, we use a normal score transformation (Chilès and Delfiner, 2012) to normalize the de-trended topography. Finally, we also de-trend and normalize the bed elevation measurements and calculate the variogram to represent topographic roughness. The topographic trend T_{trend} is stored and will be added back to simulated de-trended subglacial topography later in the MCMC algorithm.

Equipped with the variogram, the SGS-simulated topographies can reproduce the realistic topographic roughness observed in the bed elevation measurements. In each iteration of the small-scale chain, the re-simulation with SGS is restricted to a random rectangular block (e.g. Fu and Gómez-Hernández, 2008; Hansen and others, 2012; Laloy and others, 2016) to facilitate the convergence and to satisfy the inter-dependency requirement of MCMC. In each MCMC iteration, we select the block's center at a random location within the high-velocity region and sample the block's lateral dimensions from a uniform distribution between 2 km and 8 km (Fig. 6, step 3.1), which we tuned to achieve acceptance rates between 0.1 and 0.4. Inside the block, we re-simulate grid cells that are not bed elevation measurements (Fig. 6, step 3.2, 3.3). The simulation is conditioned to bed elevation measurements inside the block and neighboring

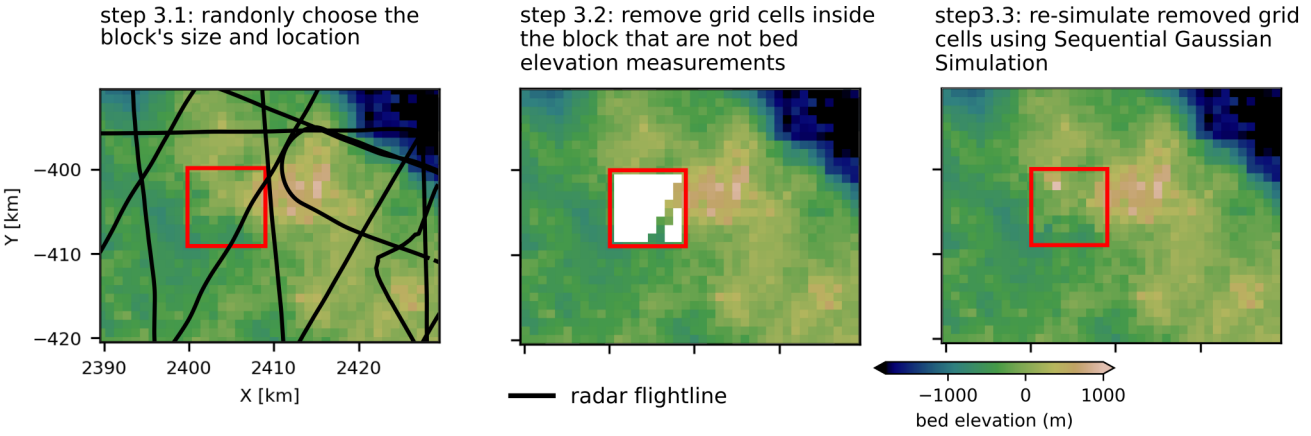

Fig. 6. The figure expands on the step 3 in Fig. 4b. An illustration of the update method used in the small-scale chain. The red rectangle represents the selected random block.

subglacial topography outside the block. The topography is then back-transformed and added back to the trend so the mass flux residuals and acceptance probability can be calculated.

The subglacial topography outside the high-velocity region is not masked out in the block-based SGS simulations. Because of the block's small size and its central location within the high-velocity region, it only changes grid cells within approximately 4–5 km of the high-velocity region. This design effectively created a 'buffer' zone such that the mass flux residuals are efficiently minimized at the margin of the high-velocity region and the topography merges smoothly with the low-velocity region. The calculation of mass flux residuals, however, is still restricted to be within the high-velocity region.

Generate the topography ensemble

While the two-phase perturbation strategy deviates from traditional MCMC implementations, the algorithm retains the fundamental structure of a Bayesian inversion. The geostatistical prior defines plausible spatial correlations, and the physical model acts as a constraint via the likelihood. We explore the posterior through repeated perturbation and acceptance/rejection steps based on the mass flux residuals.

We designed a combination of large-scale and small-scale chains to generate the final ensemble of topography realizations. First, for Denman Glacier, we initiate 4 large-scale chains with different initial topographies, which are simulated using SGS conditioned on the quality-controlled bed elevation measurements (Fig. 4a, step 1). For Totten Glacier, we initialize 2 large-scale chains with the same process. After the large-scale topographic features stabilize, we smooth the mean topography of the large-scale chain to obtain the topographic trend. We also sample 10 subglacial topography realizations from each large-scale

chain to be used as the initial topography to start the small-scale chains. Next, we run 10 small-scale chains with detrended, normalized subglacial topography. Each small-scale chain runs until $\sim 80\%$ of the grid cells inside the high-velocity region have been updated at least once. One topography realization is sampled at the end of each small-scale chain. In total, Denman Glacier has 4 large-scale chains that diverge into 40 small-scale chains, which provide an ensemble of 40 topography realizations. Totten Glacier has 2 large-scale chains and 20 following small-scale chains, providing an ensemble of 20 topography realizations.

RESULTS

We compare the subglacial topographies generated by BedMachine, SGS, and our mass-conserving MCMC approach, with their respective mass flux residuals at each grid cell (Fig. 7, Fig. 8). For Denman Glacier, both BedMachine and MCMC construct a trough deeper than -3500 m beneath the main trunk of Denman Glacier (Fig. 7a,c). In contrast, SGS simulates bed elevations between -1000 to 0 m at the same location due to the lack of bed elevation measurements in the deep trough (Fig. 7b). Similarly, for the Totten Glacier, the large-scale structures in the MCMC-generated topographies more closely resemble BedMachine than the SGS-generated topography. (Fig. 8). Besides the overall similarity, we also observe different large-scale features in BedMachine and the MCMC-sampled topography. For instance, BedMachine shows a 2 km-deep, 30 km-long depression upstream of Denman Glacier (northing -340 km and easting 2350 km), which does not exist in the MCMC-sampled topography.

Fig. 9 shows the sum of squares of mass flux residuals in the 4 large-scale chains and the following 40 small-scale chains used for simulating Denman Glacier subglacial topography. Similarly, Fig. 10 shows the reduction of mass flux residuals in 2 large-scale chains and 20 small-scale chains for Totten Glacier. The bold lines in these two figures highlight a large-scale chain and a following small-scale chain for Denman and Totten Glacier, respectively. The large-scale chains are initiated by the topography in Fig. 7b or Fig. 8c and with large mass flux residuals. After iterative perturbations and simulations, the end topographies in the small-scale chain (Fig. 7c, Fig. 8c) reduced the residuals by one order of magnitude. The realizations assembled in the final ensemble, presented as orange dots in Fig. 9 and Fig. 10, have sums of squares of mass flux residuals slightly lower than the one calculated for BedMachine.

We quantify and compare the topographic roughness by presenting the empirical variograms for the topographies, where smaller semi-variances at the same lag distances indicate a smoother topography (Fig. 11). The bed elevation measurements, SGS-generated topography, and members in the MCMC-generated

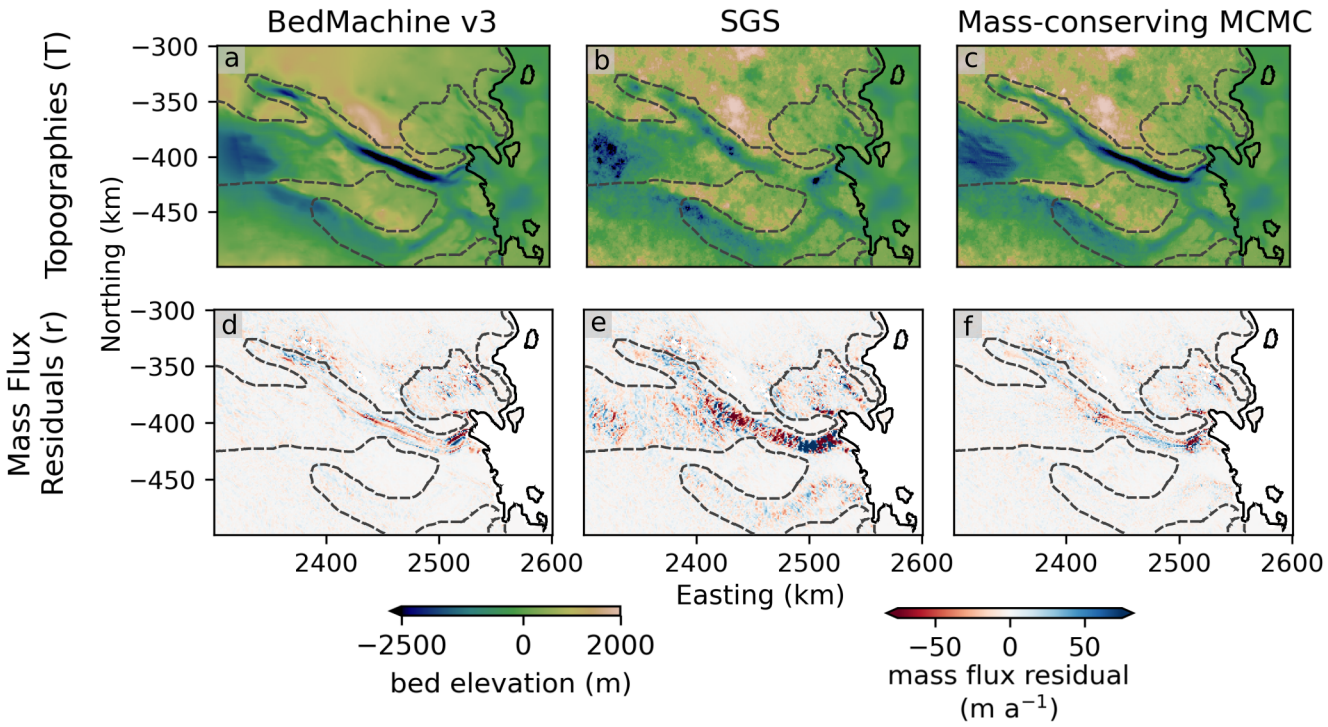

Fig. 7. Subplots a, b, c show Denman subglacial topographies generated by different methods, where subplots d, e, f present the associated mass flux residuals. The dashed gray line and the solid black lines represent high-velocity region and grounding line of Denman Glacier, respectively. The mean of the absolute mass flux residuals inside the high-velocity regions for d, e, f is respectively 5.86, 14.48, and 5.78. The SGS-generated subglacial topography at subplot b is used to initialize one of the large-scale chains for Denman Glacier.

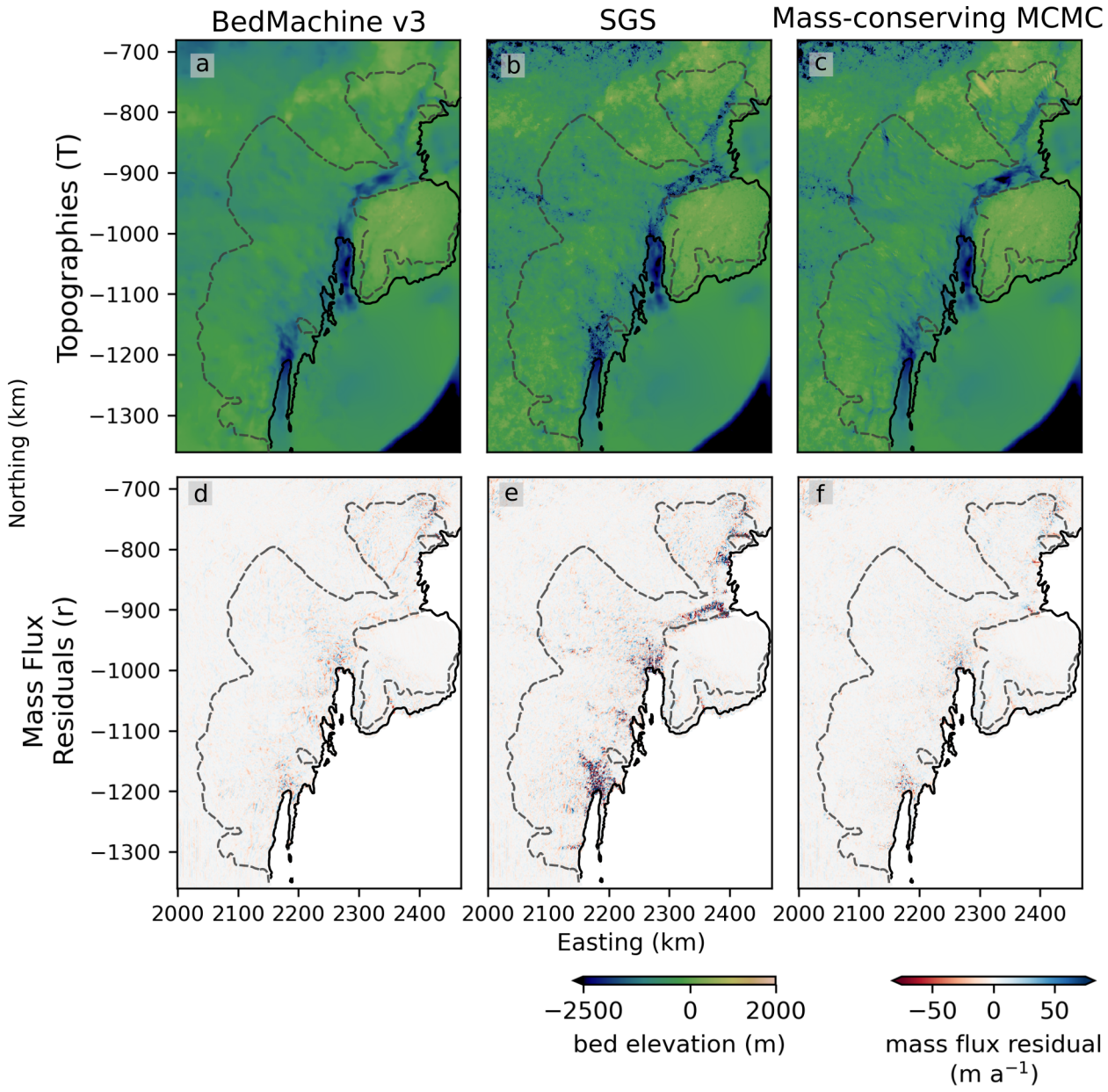

Fig. 8. This figure shows the same data as Figure 7 but for the Totten Glacier. Subplots a, b, c show topographies generated by different methods, and subplots d, e, f show the associated mass flux residuals. The dashed gray line and the solid black lines represent high-velocity region and grounding line for Totten Glacier, respectively. The mean of the absolute mass flux residuals inside the high-velocity regions for d, e, f is respectively 5.27, 9.26, and 4.66. The SGS-generated subglacial topography in subplot b is used to initiate one of the large-scale chains for Totten Glacier.

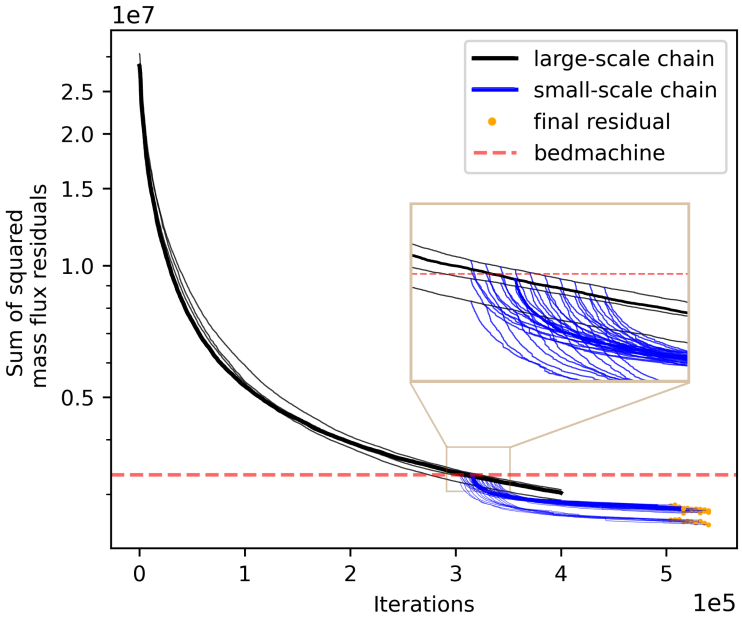

Fig. 9. The sum of squares of mass flux residuals in the 4 large-scale chains and the corresponding 40 small-scale chains used for simulating Denman subglacial topography. The bold lines show an example of large-scale chains and an example of small-scale chains. The orange dots denote the end sum of squared residuals of each topography realizations in the ensemble. The transition between large-scale chains and small-scale chains is enlarged in the inset figure.

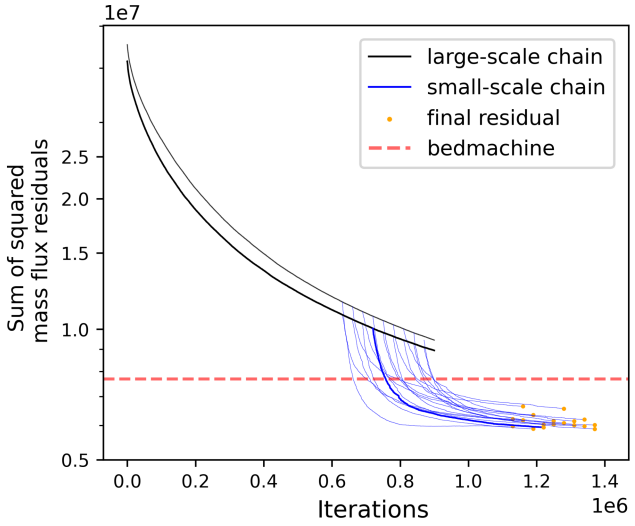

Fig. 10. The sum of squares of mass flux residuals in the 2 large-scale chains and the corresponding 20 small-scale chains used in Totten case study. The bold lines show an example of large-scale chains and an example of small-scale chains. The orange dots at the end of the lines denote the end sum of squared residuals of each topography realizations in the ensemble.

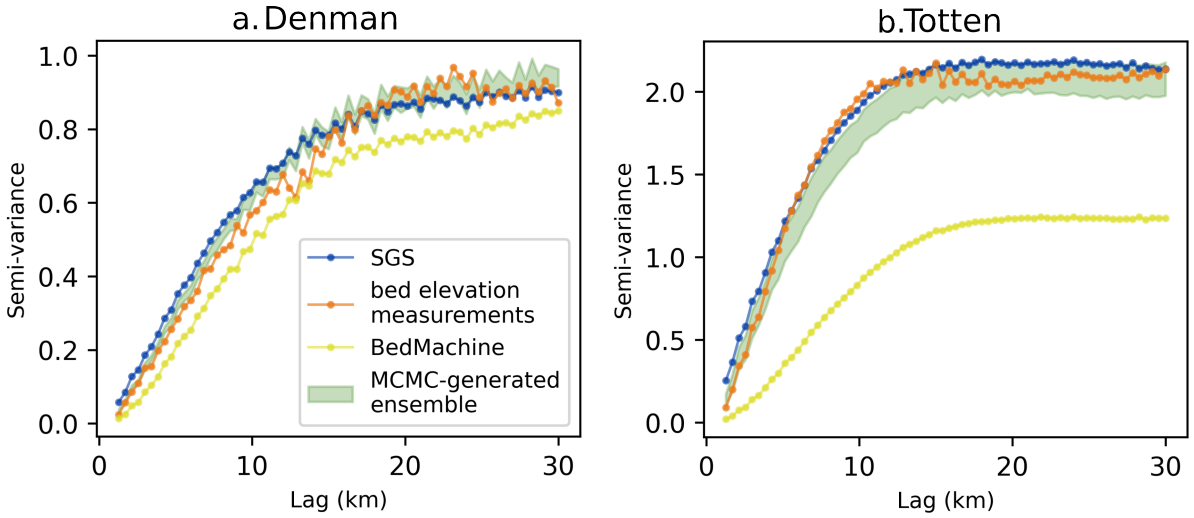

Fig. 11. Comparison of variograms calculated from detrended, normalized BedMachine, one SGS-generated subglacial topography, and MCMC-generated topographies in the high-velocity region and detrended, normalized bed elevation measurements in the entire study region. The trend used for de-trending is calculated by interpolating bed elevation measurements through a radial basis function interpolator with a thin-plate-spline kernel. Subplot a shows variograms calculated in Denman Glacier, whereas subplot b shows variograms in Totten Glacier.

ensemble have a similar topographic roughness, whereas BedMachine has a smoother topography. All MCMC-generated ensemble members also have similar roughness that is close to the roughness in bed elevation measurements. For Totten Glacier, the MCMC-generated topographies have slightly less variance compared to bed elevation measurements.

We present the mean and the two standard deviations of the topography ensemble. In the ensemble mean (Fig. 12a, Fig. 13a), we observe some consistent topographic features across different chains. The spatially-averaged standard deviation of the ensemble is $\sim$ 45 m inside the high-velocity region of Denman Glacier (Fig. 12b) and $\sim$ 41 m inside the high-velocity region of Totten Glacier (Fig. 13b). The standard deviation tends to be larger in areas with fewer radar flight lines. Outside the high-velocity region, the subglacial topography is not perturbed by MCMC, thus only represents ensemble statistics from the 4 SGS-generated topographies used to initialize large-scale chains for Denman Glacier and the 2 SGS-generated topographies for Totten Glacier. Fig. 12c shows the differences between the ensemble mean topography and the BedMachine topography in Denman, which is less than 500 m across most areas but reaches 2000 m at some locations, such as at northing 340 km and easting 2350 km. For Totten, the differences between ensemble mean and the BedMachine reaches nearly 1000 m (Fig. 13). BedMachine provides the maximum error of bed elevation (Fig. 12d, Fig. 13d), which represents how the assumed maximum errors in the ice velocity, surface mass balance, and surface elevation change rate could cause variations in the BedMachine

topography solution. Comparing the ensemble standard deviation (Fig. 12c, Fig. 13c) and the maximum bed topography error provided by BedMachine (Fig. 12d, Fig. 13d), we observe that the difference between the ensemble mean and BedMachine exceeds the BedMachine error bound, especially in the vicinity of the Denman trough.

To reveal the details of various topography realizations in the ensemble, we present several cross-sections in the high-velocity region (Fig. 14, Fig. 15). Fig. 14 shows the different geometry of the Denman trough reconstructed by MCMC and BedMachine, where the maximum difference exceeds 1 km (e.g., Fig. 14a, b). Among cross-sections in Fig. 14, the spread of the bed elevation distribution changes across the region (Fig. 14c, d, e). The topography ensemble has a smaller elevation range ($\sim$ 200 m) within the trough (Fig. 14a) and upstream of the trough (Fig. 14b, between 40 and 100 km along-profile distance). In comparison, we find topographic uncertainty to be more than 500 m near the grounding line (Fig. 14c between 17 and 24 km along-profile distance) and in the inland basin (Fig. 14d). For cross-sections of the high-velocity region of Totten Glacier, the elevation spread of MCMC-generated subglacial topographies in data-rich regions (e.g. Fig. 15 a, c) is drastically different from locations with less bed elevation measurements (e.g. Fig. 15b, d). In particular, Fig. 15d shows a region where the elevation differences between the ensemble members exceed 3000 m.

DISCUSSION

In this paper, we present a new geostatistical inversion method, which was used to sample the distribution of subglacial topography at Denman Glacier and Totten Glacier. The final topography ensemble validates the existence of different subglacial topography realizations that are mass-conserving, realistically rough, and constrained by bed elevation measurements.

The ensemble statistics and the cross-sections (Fig. 12, 13, 14, 15) illustrate the potential of stochastic methods in quantifying the topographic uncertainty in high-velocity regions. The sampled topography realizations have similar sums of squared mass flux residuals (Fig. 9, Fig. 10) while presenting distinct topographic features. The elevation differences between realizations are substantial and spatially varying, ranging from 10^2 to 10^3 meters in different locations (Fig. 14, Fig. 15). The complex distribution of bed elevation, simulated by the MCMC algorithm, shows diverse variable topographic features and contrasts with the random topographic perturbations typically used to test the sensitivity of ice-sheet models to subglacial topography (e.g. Sun and others, 2014; Castleman and others, 2022; Bulthuis and Larour, 2022;

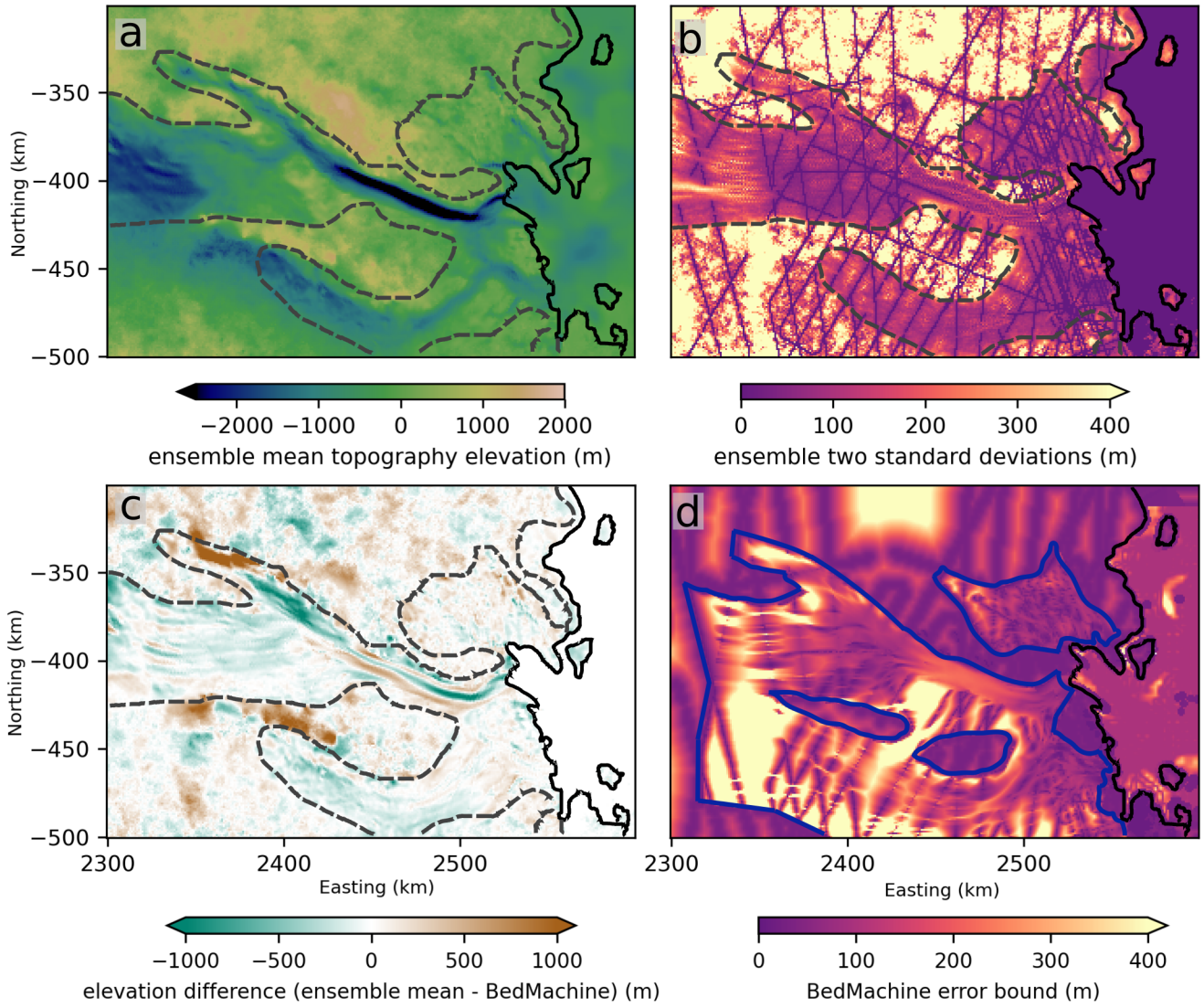

Fig. 12. This figure presents MCMC-generated ensemble for Denman Glacier and the comparison to BedMachine. Subplot a shows ensemble mean bed elevation (m); b shows the ensemble standard deviation multiplied by two (m); c shows the elevation difference (ensemble mean minus BedMachine; m); d shows the error bound of the BedMachine topography. In a, b, and c, the dashed gray outlines denote the high-velocity region. In d, the dark blue outlines denote regions where BedMachine use mass conservation approach to invert for subglacial topography.

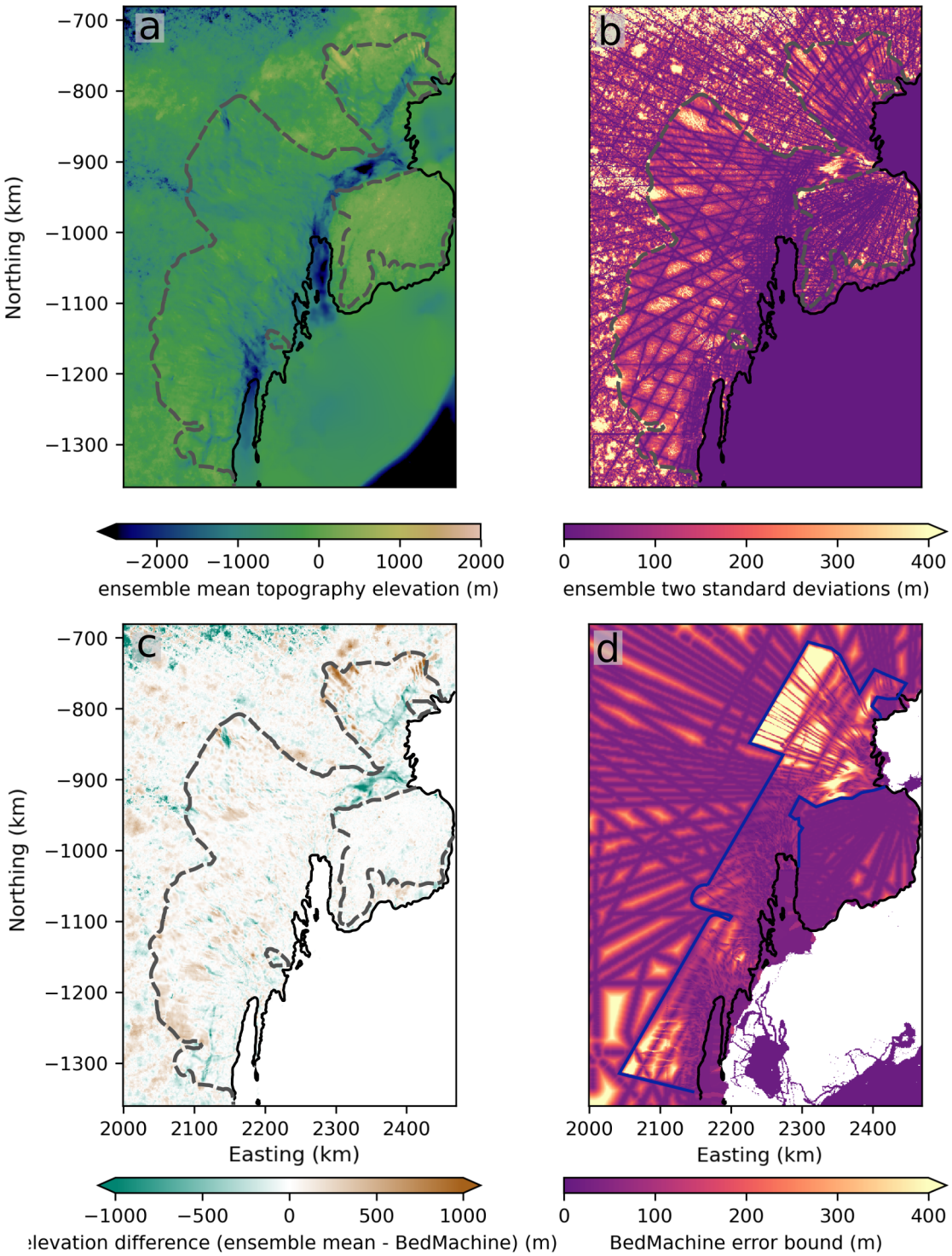

Fig. 13. This figure plots the same data as Fig. 12 but for Totten Glacier. Subplot a shows ensemble mean bed elevation (m); b shows the ensemble standard deviation multiplied by two (m); c shows the elevation difference (ensemble mean minus BedMachine; m); d shows the error bound of the BedMachine topography. The solid black lines mark grounding lines. In a, b, and c, the dashed gray outlines denote the high-velocity region. In d, the dark blue outlines denote regions where BedMachine use mass conservation approach to invert for subglacial topography.

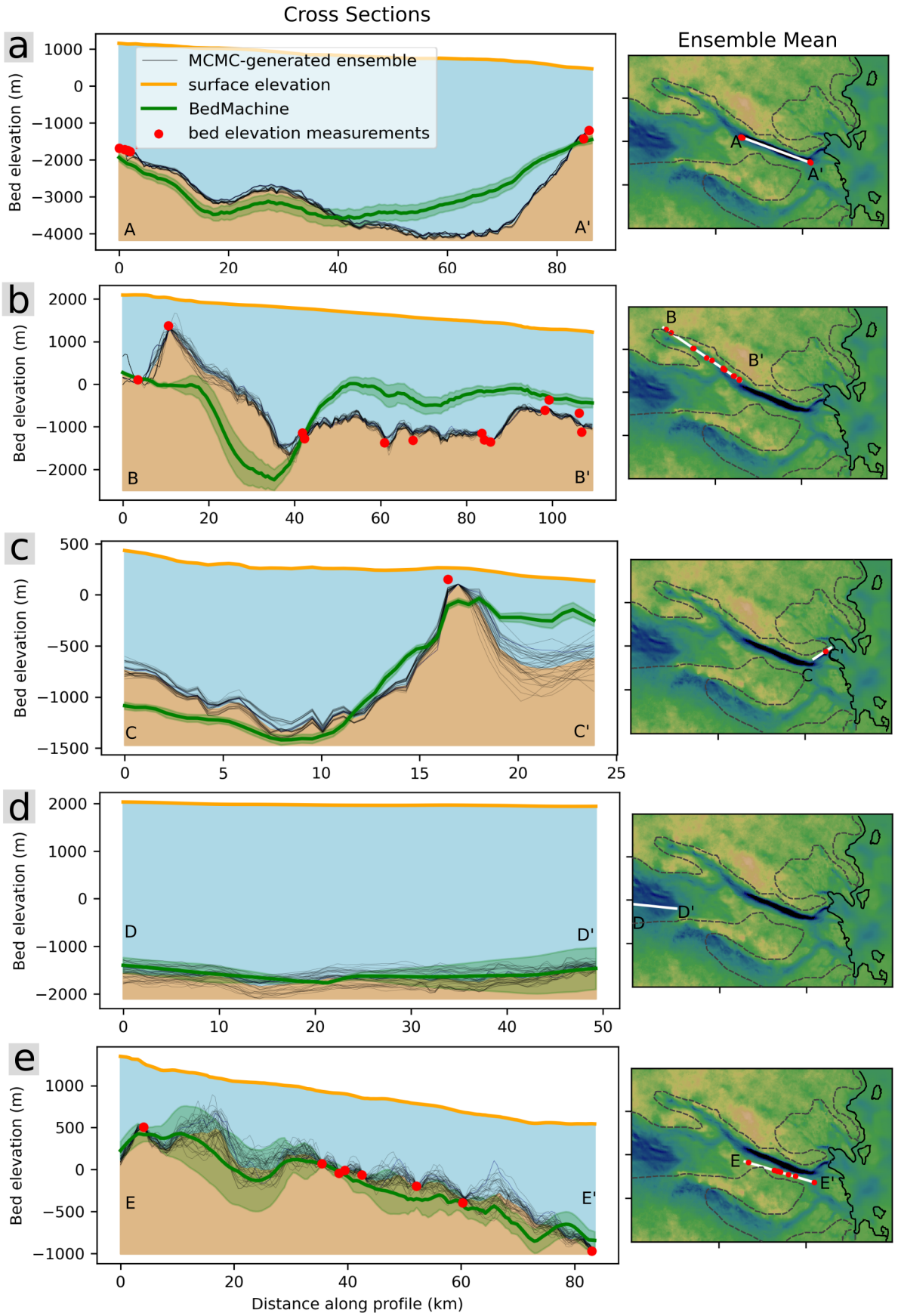

Fig. 14. The left column shows subglacial topography cross-sections of Denman Glacier. The semi-transparent green envelope indicates BedMachine error bounds, and the upper limit of the brown region marks the mean of the MCMC-generated topographies. Axes use different scales, so cross-subplot comparisons require caution. The right column shows transect locations and the mean of the MCMC-generated topographies of Denman Glacier. Bed elevations are projected onto transects by linear interpolation, while bed elevation measurements are projected using nearest-neighbor interpolation.

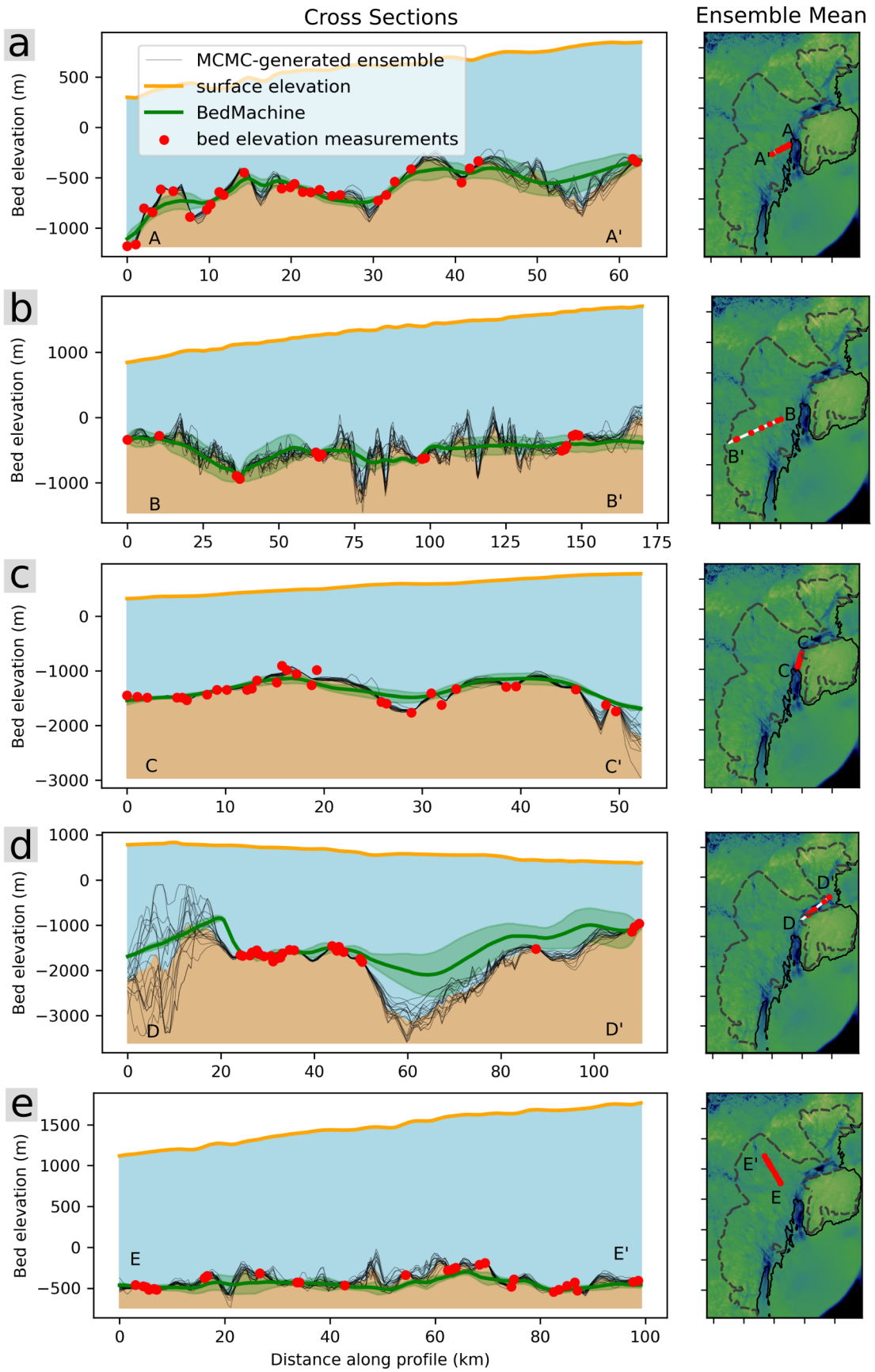

Fig. 15. This figure shows cross-sections of subglacial topographies generated for Totten Glacier, similar to Fig. 14. The left column shows subglacial topography cross-sections. The semi-transparent green envelope indicates BedMachine error bounds, and the upper limit of the brown region marks the mean of the MCMC-generated topographies. Axes use different scales, so cross-subplot comparisons require caution. The right column shows transect locations and the mean of the MCMC-generated topographies. Bed elevations are projected onto transects by linear interpolation, while bed elevation measurements are projected using nearest-neighbor interpolation.

Wernecke and others, 2022).

The diverse small-scale topographic features generated in the MCMC could impact modeling of ice dynamics. Subglacial topography is a critical component in many glacial processes, affecting ice deformation patterns (Meyer and Creyts, 2017; Law and others, 2023; Liu and others, 2024), subglacial water routing (Zuo and others, 2020; MacKie and others, 2021b), and stability of the glaciers (Gasson and others, 2015; Wernecke and others, 2022). The complex interactions between topographic uncertainty and ice stream dynamics is often studied via ensemble modeling (e.g. Robel and others, 2019; Aschwanden and others, 2019; Albrecht and others, 2020; Bulthuis and others, 2019). Our method generates topography realizations that can be easily incorporated into an ensemble of models, thus enabling the propagation of topographic uncertainties. As subglacial topography is found to be one of the most influential factors in the prediction of ice-sheet contribution to sea level (Castleman and others, 2022), sea level uncertainty cannot be robustly quantified without the propagation of topographic uncertainty.

On the other hand, inversions of englacial and subglacial geophysical parameters, such as ice viscosity or sliding coefficient, often require a known subglacial topography. Most conventional inversions treat subglacial topography as a single deterministic map (Morlighem and others, 2010; Pollard and DeConto, 2012), which would cause the inversions to compensate for errors in subglacial topography (Kyrke-Smith and others, 2018; Hoffman and others, 2022; Rathmann and Lilien, 2022; Berends and others, 2023). An ensemble of topography realizations can be used in an ensemble of inversions to explore how the inverted parameters compensate for topographic uncertainty.

Previous researches have found that both topographic roughness (Law and others, 2023; Liu and others, 2024) and topographic uncertainties (Wernecke and others, 2022) directly affect ice dynamics and ice-sheet evolutions. Our methods provide a mean to simulate uncertain small-scale topographic features while controlling the topographic roughness. The resulting subglacial topography ensemble can be used to study and compare the effects of topographic roughness and topographic features' variability in ice sheet models.

Additionally, by quantifying uncertainties in mass-conserving topography, we can identify areas within high-velocity regions where bed elevations remain poorly constrained and contribute disproportionately to ice-sheet model uncertainty, which would help guide future radar campaigns.

Subglacial topographies reconstructed by different methods show different large-scale features. While SGS reconstructs realistically-rough subglacial topographies based on the bed elevation measurements, SGS samples insufficiently when the true bed elevation values in the data gap differ greatly from the surround-

ing topography (Fig. 7b, Fig. S4). The MCMC method first finds large-scale topographic trends that are necessary for mass conservation, and then re-simulates small-scale topographic variations. This is shown in Fig. 7 where the high-relief Denman trough is reconstructed by both MCMC and BedMachine, and the SGS-generated topographies consistently reconstruct a shallow trough based on neighboring bed elevation measurements. On the other hand, the difference between MCMC-sampled topographies and BedMachine topography often exceeds the topographic error bound in BedMachine and the two standard deviation in the MCMC-ensemble (Fig. 14a, b, c, Fig.13b, d). Several factors could contribute to this difference. First, the MCMC method does not restrict the topography's gradients when generating the large-scale trends, whereas BedMachine solves for smooth topographic features (Morlighem and others, 2020). This additional smoothness requirement in BedMachine could change the solution to mass conservation. Second, the MCMC-sampled topographies strictly retain bed elevation measurements, whereas BedMachine allows deviations from the measurements. The bed elevation measurements could constrain neighboring topography when combined with mass conservation. We suggest that future research could investigate how deviating from bed elevation measurements affects topography solutions, potentially through geostatistical simulation methods that incorporate uncertainties in data (e.g., Hansen and others, 2018).

We demonstrated the application of the MCMC method to generate subglacial topography of the high-velocity regions of Denman and Totten Glacier. The two regions represent different subglacial topography regimes, where Denman Glacier is featured by high-relief subglacial trough, and Totten Glacier is characterized by gradual elevation change. Overall, the two-step approach provides a flexible workflow to accommodate both large-scale and small-scale topographic features and could easily be applied to other glaciers. Because this mass conservation approach assumes ice velocity is dominated by sliding, our method is only suitable for high-velocity regions. For low-velocity regions, geostatistical simulation remains a better alternative (e.g. MacKie and others, 2023). Future studies where the depth-averaged velocity is modeled as a fraction of surface velocities could potentially help to extend the application region of our mass conservation method (e.g. Brinkerhoff and others, 2016; Teisberg and others, 2021).

In addition, our methods can be used for simulation subglacial topography with a resolution higher than 1 km. But increasing topographic resolution inevitably increases the number of grid cells to updates for, which may require more MCMC iterations. The development of efficient geostatistics inversion algorithm with possibility of parallel computing is discussed in the last paragraph of the Discussion section.

When applying this method to a large region, it is important to consider the spatial heterogeneity

of topographic roughness. Topographic roughness and anisotropy of topographic features naturally vary based on the substrate's lithology and weathering process. In the current test, we used one variogram to characterize the topographic spatial structure across each study area. In future studies, sub-regions with different topographic roughness and anisotropic angles could be partitioned, where different variograms could be used to simulate topography realizations with spatially varying roughness (e.g. MacKie and others, 2023). The flexibility of MCMC allows the multi-variograms approach to be easily incorporated into the current implementation of the method.

In the current method, the distributions of mass flux residuals are approximated using mass flux residuals calculated from BedMachine topography. Since the mass flux residuals distribution is determined by uncertainties in ice velocity, surface mass balance, and surface elevation (Supplementary Material Section 3), reduced data uncertainty could allow a closer approximation to $r = 0$. On the other hand, we also suggest several approaches that can be used to accurately represent the distribution of mass flux residuals. Brinkerhoff and others (2016) adopt an MCMC method that infers ice velocity from the topography in each iteration and compares the inferred velocity with the observed velocity. This approach allows the incorporation of velocity uncertainty into the inversion of subglacial topography. However, this method was only demonstrated on a 2D flow line (Brinkerhoff and others, 2016), where velocity can be easily calculated from topography using mass conservation. Another approach is to jointly simulate observational data and subglacial topography. For example, we could invert for pairs of depth-averaged velocity and subglacial topography such that they produce ice flux divergences that are within the uncertainties in surface mass balance and surface elevation change rate. However, this approach could significantly increase the computational cost and would delay the Markov chain's convergence. We suggest that with a better understanding of uncertainties in the observed data and advanced MCMC techniques designed for sampling high-dimensional parameters (e.g. Laloy and others, 2016; Reuschen and others, 2021), these possible solutions can be studied further.

The high computational cost of generating topography ensembles can be reduced with parallel computing, machine learning, and improved MCMC design. In our current approach, 40 realizations of Denman Glacier subglacial topography are obtained by running 4 large-scale and 40 small-scale chains sequentially, requiring nearly two weeks of runtime on a Mac Studio with Apple M1 Ultra chip and 128 GB memory. A reduction of runtime could be achieved through parallelization of independent Markov chains (Gelman and Rubin, 1992). In addition, machine learning methods could be employed as time-efficient surrogates

to generate geostatistical simulations (Laloy and others, 2018; Bai and Tahmasebi, 2022), which is the most time-consuming component in the current workflow. Finally, advanced MCMC techniques designed for sampling high-dimensional parameters (e.g. Laloy and others, 2016; Reuschen and others, 2021) could facilitate the Markov chain's convergence and reduce the number of iterations required, which is especially valuable when inverting for large regions of high-resolution subglacial topography.

CONCLUSION

Reconstructing subglacial topography from sparse bed elevation measurements presents difficulties in preserving realistic topographic roughness and ensuring physical consistency with surface observations. In this study, we develop a novel geostatistical MCMC method for stochastically simulating subglacial topography and test the method on Denman Glacier and Totten Glacier. We successfully simulate an ensemble of mass-conserving, realistically rough, and radar-constrained topography realizations. The simulated topographies show large differences to the numerically solved topography in BedMachine. The topography ensemble also presents spatially varying topographic uncertainty and distinct large-scale and small-scale topographic features across realizations. We demonstrated the application of geostatistical MCMC in the inversion of subglacial topography. Furthermore, the topography ensemble generated provides an opportunity to quantify the impact of topographic uncertainty on ice-sheet modeling and sea-level-rise projections.

DATA AVAILABILITY

The simulated topography ensemble that support the findings of this study is openly available in U.S. Antarctic Program Data Center, which can be found at https://doi.org/10.15784/601927.

SUPPLEMENTARY MATERIAL

The Supplementary Material is attached in the submission.

COMPETING INTERESTS

The authors have no competing interests to declare

ACKNOWLEDGMENT

N.S., E.J.M., and M.J.F. were supported by NSF award 2324092. N.S. was also supported by the research fellowship under Department of Geological Sciences, University of Florida. F.S.M. was supported under an Australian Research Council (ARC) Discovery Early Career Research Award (DECRA; DE210101433) and the ARC Special Research Initiative Securing Antarctica's Environmental Future (SR200100005).

REFERENCES

Aitken ARA, Roberts JL, van Ommen TD, Young DA, Golledge NR, Greenbaum JS, Blankenship DD and Siegert MJ (2016) Repeated large-scale retreat and advance of Totten Glacier indicated by inland bed erosion. *Nature*, **533**(7603), 385–389 (doi: 10.1038/nature17447)

Albrecht T, Winkelmann R and Levermann A (2020) Glacial-cycle simulations of the Antarctic Ice Sheet with the Parallel Ice Sheet Model (PISM) – Part 2: Parameter ensemble analysis. *The Cryosphere*, **14**(2), 633–656 (doi: 10.5194/tc-14-633-2020)

Aschwanden A, Fahnestock MA, Truffer M, Brinkerhoff DJ, Hock R, Khroulev C, Mottram R and Khan SA (2019) Contribution of the Greenland Ice Sheet to sea level over the next millennium. *Science Advances*, **5**(6), eaav9396 (doi: 10.1126/sciadv.aav9396)

Bai T and Tahmasebi P (2022) Sequential Gaussian simulation for geosystems modeling: A machine learning approach. *Geoscience Frontiers*, **13**(1), 101258 (doi: 10.1016/j.gsf.2021.101258)

Berends CJ, van de Wal RSW, van den Akker T and Lipscomb WH (2023) Compensating errors in inversions for subglacial bed roughness: same steady state, different dynamic response. *The Cryosphere*, **17**(4), 1585–1600 (doi: 10.5194/tc-17-1585-2023)

Bianchi C, Cafarella L, De Michelis P, Forieri A, Frezzotti M, Tabacco IE and Zirizzotti A (2003) Radio Echo Sounding (RES) investigations at Talos Dome (East Antarctica): bedrock topography and ice thickness. *Annals of Geophysics*, **46**(6), 1265–1270 (doi: 10.4401/ag-3471)

Bingham RG, Vaughan DG, King EC, Davies D, Cornford SL, Smith AM, Arthern RJ, Brisbourne AM, De Rydt J, Graham AGC, Spagnolo M, Marsh OJ and Shean DE (2017) Diverse landscapes beneath Pine Island Glacier influence ice flow. *Nature Communications*, **8**(1), 1618 (doi: 10.1038/s41467-017-01597-y)

Blankenship D, Kempf S, Young D, Richter T, Schroeder D, Greenbaum J, van Ommen T, Warner R, Roberts J, Young N, Lemeur E, Siegert M and Holt J (2017) IceBridge HiCARS 1 L1B time-tagged echo strength profiles, version 1 (doi: 10.5067/W2KXX0MYNJ9G)

687 Bradwell T, Small D, Fabel D, Smedley RK, Clark CD, Saher MH, Callard SL, Chiverrell RC, Dove D, Moreton SG,
688 Roberts DH, Duller GAT and Cofaigh CO (2019) Ice-stream demise dynamically conditioned by trough shape and
689 bed strength. *Science Advances*, **5**(4), eaau1380 (doi: 10.1126/sciadv.aau1380)

690 Brinkerhoff DJ, Aschwanden A and Truffer M (2016) Bayesian inference of subglacial topography using mass con-
691 servation. *Frontiers in Earth Science*, **4** (doi: 10.3389/feart.2016.00008)

692 Bulthuis K and Larour E (2022) Implementation of a Gaussian Markov random field sampler for forward uncertainty
693 quantification in the Ice-sheet and Sea-level System Model v4.19. *Geoscientific Model Development*, **15**(3), 1195–
694 1217 (doi: 10.5194/gmd-15-1195-2022)

695 Bulthuis K, Arnst M, Sun S and Pattyn F (2019) Uncertainty quantification of the multi-centennial response of the
696 Antarctic ice sheet to climate change. *The Cryosphere*, **13**(4), 1349–1380 (doi: 10.5194/tc-13-1349-2019)

697 Castleman BA, Schlegel NJ, Caron L, Larour E and Khazendar A (2022) Derivation of bedrock topography mea-
698 surement requirements for the reduction of uncertainty in ice-sheet model projections of Thwaites Glacier. *The*
699 *Cryosphere*, **16**(3), 761–778 (doi: 10.5194/tc-16-761-2022)

700 Chilès JP and Delfiner P (2012) *Geostatistics: modeling spatial uncertainty*. John Wiley & Sons, Incorporated,
701 Newark, 2 edition, ISBN 9781118136188 (doi: 10.1002/9781118136188)

702 Colgan W, MacGregor JA, Mankoff KD, Haagenson R, Rajaram H, Martos YM, Morlighem M, Fahnestock MA
703 and Kjeldsen KK (2021) Topographic correction of geothermal heat flux in Greenland and Antarctica. *Journal of*
704 *Geophysical Research: Earth Surface*, **126**(2), e2020JF005598 (doi: 10.1029/2020JF005598)

705 Deutsch C and Journel A (1992) Geostatistical software library and user's guide. *Oxford University Press*, **8**(91)

706 Dow CF, McCormack FS, Young DA, Greenbaum JS, Roberts JL and Blankenship DD (2020) Totten Glacier sub-
707 glacial hydrology determined from geophysics and modeling. *Earth and Planetary Science Letters*, **531**, 115961
708 (doi: 10.1016/j.epsl.2019.115961)

709 Farinotti D, King EC, Albrecht A, Huss M and Gudmundsson GH (2014) The bedrock topography of Starbuck
710 Glacier, Antarctic Peninsula, as determined by radio-echo soundings and flow modeling. *Annals of Glaciology*,
711 **55**(67), 22–28 (doi: 10.3189/2014AoG67A025)

712 Foerste C, Flechtner F, Schmidt R, Meyer U, Stubenvoll R, Barthelmes F, Rothacher M, Biancale R, Bruinsma S
713 and Lemoine J (2005) A new high resolution global gravity field model from the combination of grace satellite
714 mission and altimetry/gravimetry surface gravity data. In *Geophysical Research Abstracts*, volume 7, 04561

715 Foerste C, Bruinsma SL, Abrykosov O, Lemoine JM, Marty JC, Flechtner F, Balmino G, Barthelmes F and Biancale
716 R (2014) EIGEN-6C4 The latest combined global gravity field model including GOCE data up to degree and order
717 2190 of GFZ Potsdam and GRGS Toulouse. (doi: 10.1029/2022JF007040)

718 Forte E, Bondini MB, Bortoletto A, Dossi M and Colucci RR (2019) Pros and cons in helicopter-borne GPR data
719 acquisition on rugged mountainous areas: Critical analysis and practical guidelines. *Pure and Applied Geophysics*,
720 **176**(10), 4533–4554 (doi: 10.1007/s00024-019-02196-2)

721 Frémand AC, Fretwell P, Bodart JA, Pritchard HD, Aitken A, Bamber JL, Bell R, Bianchi C, Bingham RG, Blanken-
722 ship DD, Casassa G, Catania G, Christianson K, Conway H, Corr HFJ, Cui X, Damaske D, Damm V, Drews R,
723 Eagles G, Eisen O, Eisermann H, Ferraccioli F, Field E, Forsberg R, Franke S, Fujita S, Gim Y, Goel V, Gogineni
724 SP, Greenbaum J, Hills B, Hindmarsh RCA, Hoffman AO, Holmlund P, Holschuh N, Holt JW, Horlings AN,
725 Humbert A, Jacobel RW, Jansen D, Jenkins A, Jokat W, Jordan T, King E, Kohler J, Krabill W, Kusk Gillespie
726 M, Langley K, Lee J, Leitchenkov G, Leuschen C, Luyendyk B, MacGregor J, MacKie E, Matsuoka K, Morlighem
727 M, Mouginot J, Nitsche FO, Nogi Y, Nost OA, Paden J, Pattyn F, Popov SV, Rignot E, Rippin DM, Rivera A,
728 Roberts J, Ross N, Ruppel A, Schroeder DM, Siegert MJ, Smith AM, Steinhage D, Studinger M, Sun B, Tabacco I,
729 Tinto K, Urbini S, Vaughan D, Welch BC, Wilson DS, Young DA and Zirizzotti A (2023) Antarctic Bedmap data:
730 Findable, Accessible, Interoperable, and Reusable (FAIR) sharing of 60 years of ice bed, surface, and thickness
731 data. *Earth System Science Data*, **15**(7), 2695–2710 (doi: 10.5194/essd-15-2695-2023)

732 Fretwell P, Pritchard HD, Vaughan DG, Bamber JL, Barrand NE, Bell R, Bianchi C, Bingham RG, Blankenship DD,
733 Casassa G, Catania G, Callens D, Conway H, Cook AJ, Corr HFJ, Damaske D, Damm V, Ferraccioli F, Forsberg
734 R, Fujita S, Gim Y, Gogineni P, Griggs JA, Hindmarsh RCA, Holmlund P, Holt JW, Jacobel RW, Jenkins A,
735 Jokat W, Jordan T, King EC, Kohler J, Krabill W, Riger-Kusk M, Langley KA, Leitchenkov G, Leuschen C,
736 Luyendyk BP, Matsuoka K, Mouginot J, Nitsche FO, Nogi Y, Nost OA, Popov SV, Rignot E, Rippin DM, Rivera
737 A, Roberts J, Ross N, Siegert MJ, Smith AM, Steinhage D, Studinger M, Sun B, Tinto BK, Welch BC, Wilson
738 D, Young DA, Xiangbin C and Zirizzotti A (2013) Bedmap2: improved ice bed, surface and thickness datasets for
739 antarctica. *The Cryosphere*, **7**(1), 375–393 (doi: 10.5194/tc-7-375-2013)

740 Fu J and Gómez-Hernández JJ (2008) Preserving spatial structure for inverse stochastic simulation using block-
741 ing Markov chain Monte Carlo method. *Inverse Problems in Science and Engineering*, **16**(7), 865–884 (doi:
742 10.1080/17415970802015781)

743 Gallagher K, Charvin K, Nielsen S, Sambridge M and Stephenson J (2009) Markov chain Monte Carlo (MCMC)
744 sampling methods to determine optimal models, model resolution and model choice for Earth Science problems.
745 *Marine and Petroleum Geology*, **26**(4), 525–535 (doi: 10.1016/j.marpetgeo.2009.01.003)

Gasson E, DeConto R and Pollard D (2015) Antarctic bedrock topography uncertainty and ice sheet stability. *Geophysical Research Letters*, **42**(13), 5372–5377 (doi: 10.1002/2015GL064322)

Gelman A and Rubin DB (1992) Inference from iterative simulation using multiple sequences. *Statistical Science*, **7**(4), 457 – 472 (doi: 10.1214/ss/1177011136)

Gelman A, Gilks WR and Roberts GO (1997) Weak convergence and optimal scaling of random walk Metropolis algorithms. *The Annals of Applied Probability*, **7**(1), 110–120 (doi: 10.1214/aoap/1034625254)

Geyer CJ (2011) *Handbook of Markov Chain Monte Carlo*. Chapman and Hall/CRC, New York, ISBN 9780429138508 (doi: 10.1201/b10905)

Goff JA, Powell EM, Young DA and Blankenship DD (2014) Conditional simulation of Thwaites Glacier (Antarctica) bed topography for flow models: Incorporating inhomogeneous statistics and channelized morphology. *Journal of Glaciology*, **60**(222), 635–646 (doi: 10.3189/2014JoG13J200)

Goovaerts P (1997) *Geostatistics for natural resources evaluation*. Oxford University Press on Demand

Hansen TM, Cordua KS and Mosegaard K (2012) Inverse problems with non-trivial priors: efficient solution through sequential Gibbs sampling. *Computational Geosciences*, **16**(3), 593–611 (doi: 10.1007/s10596-011-9271-1)

Hansen TM, Vu LT, Mosegaard K and Cordua KS (2018) Multiple point statistical simulation using uncertain (soft) conditional data. *Computers & Geosciences*, **114**, 1–10 (doi: 10.1016/j.cageo.2018.01.017)

Haran T, Klinger M, Bohlander J, Fahnestock M, Painter T and Scambos T (2018) MEaSUREs MODIS Mosaic of Antarctica 2013-2014 (MOA2014) image map, version 1. (doi: 10.5067/RNF17BP824UM)

Hastings WK (1970) Monte Carlo sampling methods using Markov chains and their applications. *Biometrika*, **57**(1), 97–109 (doi: 10.2307/2334940)

Herzfeld UC, Eriksson MG and Holmlund P (1993) On the influence of kriging parameters on the cartographic output—a study in mapping subglacial topography. *Mathematical Geology*, **25**(7), 881–900 (doi: 10.1007/BF00891049)

Hoffman AO, Christianson K, Holschuh N, Case E, Kingslake J and Arthern R (2022) The impact of basal roughness on inland Thwaites Glacier sliding. *Geophysical Research Letters*, **49**(14), e2021GL096564 (doi: 10.1029/2021GL096564)

Howat IM, Porter C, Smith BE, Noh MJ and Morin P (2019) The Reference Elevation Model of Antarctica. *The Cryosphere*, **13**(2), 665–674 (doi: 10.5194/tc-13-665-2019)

Jones GL and Qin Q (2022) Markov Chain Monte Carlo in practice. *Annual Review of Statistics and Its Application*, **9**(1), 557–578 (doi: 10.1146/annurev-statistics-040220-090158)

Kyrke-Smith TM, Gudmundsson GH and Farrell PE (2018) Relevance of detail in basal topography for basal slipperiness inversions: A case study on Pine Island Glacier, Antarctica. *Frontiers in Earth Science*, **6** (doi: 10.3389/feart.2018.00033)

Laloy E, Linde N, Jacques D and Mariethoz G (2016) Merging parallel tempering with sequential geostatistical resampling for improved posterior exploration of high-dimensional subsurface categorical fields. *Advances in Water Resources*, **90**, 57–69 (doi: 10.1016/j.advwatres.2016.02.008)

Laloy E, Hérault R, Jacques D and Linde N (2018) Training-image based geostatistical inversion using a spatial generative adversarial neural network. *Water Resources Research*, **54**(1), 381–406 (doi: 10.1002/2017WR022148)

Lapazaran JJ, Otero J, Martín-Español A and Navarro FJ (2016) On the errors involved in ice-thickness estimates I: ground-penetrating radar measurement errors. *Journal of Glaciology*, **62**(236), 1008–1020 (doi: 10.1017/jog.2016.93)

Law R, Christoffersen P, MacKie E, Cook S, Haseloff M and Gagliardini O (2023) Complex motion of Greenland Ice Sheet outlet glaciers with basal temperate ice. *Science Advances*, **9**(6), eabq5180 (doi: 10.1126/sciadv.abq5180)

Lippl S, Blindow N, Fürst JJ, Marinsek S, Seehaus TC and Braun MH (2020) Uncertainty assessment of ice discharge using GPR-derived ice thickness from Gourdon Glacier, Antarctic Peninsula. *Geosciences*, **10**(1), 12 (doi: 10.3390/geosciences10010012)

Liu EW, Räss L, Herman F, Podladchikov Y and Suckale J (2024) Spontaneous formation of an internal shear band in ice flowing over topographically variable bedrock. *Journal of Geophysical Research: Earth Surface*, **129**(4), e2022JF007040 (doi: 10.1029/2022JF007040)

Liu W, Purdon K, Stafford T, Paden J and Li X (2016) Open Polar Server (OPS)—an open source infrastructure for the cryosphere community. *ISPRS International Journal of Geo-Information*, **5**(3), 32 (doi: 10.3390/ijgi5030032)

MacGregor JA, Boisvert LN, Medley B, Petty AA, Harbeck JP, Bell RE, Blair JB, Blanchard-Wrigglesworth E, Buckley EM, Christoffersen MS, Cochran JR, Csathó BM, De Marco EL, Dominguez RT, Fahnestock MA, Farrell SL, Gogineni SP, Greenbaum JS, Hansen CM, Hofton MA, Holt JW, Jezek KC, Koenig LS, Kurtz NT, Kwok R, Larsen CF, Leuschen CJ, Locke CD, Manizade SS, Martin S, Neumann TA, Nowicki SMJ, Paden JD, Richter-Menge JA, Rignot EJ, Rodríguez-Morales F, Siegfried MR, Smith BE, Sonntag JG, Studinger M, Tinto KJ, Truffer M, Wagner TP, Woods JE, Young DA and Yungel JK (2021) The scientific legacy of NASA's Operation IceBridge. *Reviews of Geophysics*, **59**(2), e2020RG000712 (doi: 10.1029/2020RG000712)

MacKie EJ, Schroeder DM, Caers J, Siegfried MR and Scheidt C (2020) Antarctic topographic realizations and geostatistical modeling used to map subglacial lakes. *Journal of Geophysical Research: Earth Surface*, **125**(3), e2019JF005420 (doi: 10.1029/2019JF005420)

MacKie EJ, Schroeder DM, Steinbrügge G and Culberg R (2021a) Quantifying spatial relationships in ice penetrating radar measurement uncertainty through clutter simulation. In *2021 IEEE International Geoscience and Remote Sensing Symposium IGARSS*, 8688–8691 (doi: 10.1109/IGARSS47720.2021.9553045)

MacKie EJ, Schroeder DM, Zuo C, Yin Z and Caers J (2021b) Stochastic modeling of subglacial topography exposes uncertainty in water routing at Jakobshavn Glacier. *Journal of Glaciology*, **67**(261), 75–83 (doi: 10.1017/jog.2020.84)

MacKie EJ, Field M, Wang L, Yin Z, Schoedl N, Hibbs M and Zhang A (2023) GStatSim V1.0: a Python package for geostatistical interpolation and conditional simulation. *Geoscientific Model Development*, **16**(13), 3765–3783 (doi: 10.5194/gmd-16-3765-2023)

Mälicke M (2022) SciKit-GStat 1.0: a SciPy-flavored geostatistical variogram estimation toolbox written in Python. *Geoscientific Model Development*, **15**(6), 2505–2532 (doi: 10.5194/gmd-15-2505-2022)

Mariethoz G, Renard P and Caers J (2010) Bayesian inverse problem and optimization with iterative spatial resampling. *Water Resources Research*, **46**(11), W11530 (doi: 10.1029/2010WR009274)

Matsuoka K, Moholdt G, Arthur J, Bodart J, Cui X, Ferraccioli F, Forsberg R, Goel V, Jordan TA, McCormack FS, Mottram R, Pritchard HDD, Shackleton C, Tinto KJ, Boberg F, Cavitte MGP, Drews R, Dutrieux P, Ebbing J, Eisen O, Eisermann H, Gardner A, Greene CA, Holschuh N, Jamieson SSR, Kim BH, Krauzig N, Kulessa B, Leuschen CJ, Li J, Li L, Liebsch J, MacGregor JA, MacKie EJ, Mahagaonkar A, Maton J, Morlighem M, Navarro FJ, Neff PD, Otosaka IN, Pattyn F, Ruppel AS, Sanderson RJ, Seroussi H, Shepherd A, Siegfried MR, Slater T, Stroeven AP, Studinger M, Teisberg TO, Venturelli RA, Winberry PJ, Zhao C, An L, Bamber JL, Bell RE, Bingham RG, Brehmer-Moltmann J, Eagles G, Greenbaum J, Gronset JO, Lee WS, Le Meur E, Jong LM, Lindbäck K, Lidström S, Lösing M, Minowa M, Pandey M, Ray Y, Scheinert M, Schroeder D, Seehaus T, Shahateet KF, Steinhage D, Tang X, Taylor D, Verboncoeur H, Yang J and Young DA (2025) Towards an improved understanding of the Antarctic coastal zone and its contribution to future global sea level. *PrePrint. Earth and Space Science Open Archive* (doi: 10.22541/essoar.175241971.19851046)

McArthur K, McCormack FS and Dow CF (2023) Basal conditions of Denman Glacier from glacier hydrology and ice dynamics modeling. *The Cryosphere*, **17**(11), 4705–4727 (doi: 10.5194/tc-17-4705-2023)

McNabb RW, Hock R, O'Neel S, Rasmussen LA, Ahn Y, Braun M, Conway H, Herreid S, Joughin I, Pfeffer WT

and et al (2012) Using surface velocities to calculate ice thickness and bed topography: a case study at Columbia Glacier, Alaska, USA. *Journal of Glaciology*, **58**(212), 1151–1164 (doi: 10.3189/2012JoG11J249)

Metropolis N, Rosenbluth AW, Rosenbluth MN, Teller AH and Teller E (1953) Equation of state calculations by fast computing machines. *The Journal of Chemical Physics*, **21**(6), 1087–1092 (doi: 10.1063/1.1699114)

Meyer CR and Creyts TT (2017) Formation of ice eddies in subglacial mountain valleys. *Journal of Geophysical Research: Earth Surface*, **122**(9), 1574–1588 (doi: 10.1002/2017JF004329)

Morlighem M, Rignot E, Seroussi H, Larour E, Ben Dhia H and Aubry D (2010) Spatial patterns of basal drag inferred using control methods from a full-stokes and simpler models for Pine Island Glacier, West Antarctica. *Geophysical Research Letters*, **37**(14) (doi: 10.1029/2010GL043853)

Morlighem M, Rignot E, Seroussi H, Larour E, Ben Dhia H and Aubry D (2011) A mass conservation approach for mapping glacier ice thickness. *Geophysical Research Letters*, **38**(19), L19503 (doi: 10.1029/2011GL048659)

Morlighem M, Williams CN, Rignot E, An L, Arndt JE, Bamber JL, Catania G, Chauché N, Dowdeswell JA, Dorschel B, Fenty I, Hogan K, Howat I, Hubbard A, Jakobsson M, Jordan TM, Kjeldsen KK, Millan R, Mayer L, Mouginot J, Noël BPY, O'Cofaigh C, Palmer S, Rysgaard S, Seroussi H, Siegert MJ, Slabon P, Straneo F, van den Broeke MR, Weinrebe W, Wood M and Zinglersen KB (2017) BedMachine v3: Complete bed topography and ocean bathymetry mapping of Greenland from multibeam echo sounding combined with mass conservation. *Geophysical Research Letters*, **44**(21), 11,051–11,061 (doi: 10.1002/2017GL074954)

Morlighem M, Rignot E, Binder T, Blankenship D, Drews R, Eagles G, Eisen O, Ferraccioli F, Forsberg R, Fretwell P, Goel V, Greenbaum JS, Gudmundsson H, Guo J, Helm V, Hofstede C, Howat I, Humbert A, Jokat W, Karlsson NB, Lee WS, Matsuoka K, Millan R, Mouginot J, Paden J, Pattyn F, Roberts J, Rosier S, Ruppel A, Seroussi H, Smith EC, Steinhage D, Sun B, van den Broeke MR, van Ommen TD, van Wessem M and Young DA (2020) Deep glacial troughs and stabilizing ridges unveiled beneath the margins of the Antarctic ice sheet. *Nature Geoscience*, **13**(2), 132–137 (doi: 10.1038/s41561-019-0510-8)

Mosegaard K and Tarantola A (1995) Monte Carlo sampling of solutions to inverse problems. *Journal of Geophysical Research: Solid Earth*, **100**(B7), 12431–12447 (doi: 10.1029/94JB03097)

Müller S, Schüler L, Zech A and Heße F (2022) `GSTools` v1.3: a toolbox for geostatistical modelling in Python. *Geoscientific Model Development*, **15**(7), 3161–3182 (doi: 10.5194/gmd-15-3161-2022)

Neven A, Dall'Alba V, Juda P, Straubhaar J and Renard P (2021) Ice volume and basal topography estimation using geostatistical methods and ground-penetrating radar measurements: application to the Tsanfleuron and Scex Rouge glaciers, Swiss Alps. *The Cryosphere*, **15**(11), 5169–5186 (doi: 10.5194/tc-15-5169-2021)

Nilsson J, Gardner A and Paolo FS (2023) MEaSUREs ITS_LIVE Antarctic grounded ice sheet elevation change, version 1. (doi: 10.5067/L3LSVDZS15ZV)

Nunes R, Soares A, Schwedersky G, Dillon L, Guerreiro L, Caetano H, Maciel C and Leon F (2012) Geostatistical inversion of prestack seismic data. In *Ninth International Geostatistics Congress*, 1–8

Pelle T, Greenbaum JS, Ehrenfeucht S, Dow CF and McCormack FS (2024) Subglacial discharge accelerates dynamic retreat of Aurora Subglacial Basin outlet glaciers, East Antarctica, over the 21st century. *Journal of Geophysical Research: Earth Surface*, **129**(7), e2023JF007513 (doi: 10.1029/2023JF007513)

Perego M, Price S and Stadler G (2014) Optimal initial conditions for coupling ice sheet models to earth system models. *Journal of Geophysical Research: Earth Surface*, **119**(9), 1894–1917 (doi: 10.1002/2014JF003181)

Pollard D and DeConto RM (2012) A simple inverse method for the distribution of basal sliding coefficients under ice sheets, applied to Antarctica. *The Cryosphere*, **6**(5), 953–971 (doi: 10.5194/tc-6-953-2012)

Pritchard HD, Fretwell PT, Fremand AC, Bodart JA, Kirkham JD, Aitken A, Bamber J, Bell R, Bianchi C, Bingham RG, Blankenship DD, Casassa G, Christianson K, Conway H, Corr HFJ, Cui X, Damaske D, Damm V, Dorschel B, Drews R, Eagles G, Eisen O, Eisermann H, Ferraccioli F, Field E, Forsberg R, Franke S, Goel V, Gogineni SP, Greenbaum J, Hills B, Hindmarsh RCA, Hoffman AO, Holschuh N, Holt JW, Humbert A, Jacobel RW, Jansen D, Jenkins A, Jokat W, Jong L, Jordan TA, King EC, Kohler J, Krabill W, Maton J, Gillespie MK, Langley K, Lee J, Leitchenkov G, Leuschen C, Luyendyk B, MacGregor JA, MacKie E, Moholdt G, Matsuoka K, Morlighem M, Mouginot J, Nitsche FO, Nost OA, Paden J, Pattyn F, Popov S, Rignot E, Rippin DM, Rivera A, Roberts JL, Ross N, Ruppel A, Schroeder DM, Siegert MJ, Smith AM, Steinhage D, Studinger M, Sun B, Tabacco I, Tinto KJ, Urbini S, Vaughan DG, Wilson DS, Young DA and Zirizzotti A (2025) Bedmap3 updated ice bed, surface and thickness gridded datasets for Antarctica. *Scientific Data*, **12**(1), 414 (doi: 10.1038/s41597-025-04672-y)

Rathmann NM and Lilien DA (2022) Inferred basal friction and mass flux affected by crystal-orientation fabrics. *Journal of Glaciology*, **68**(268), 236–252 (doi: 10.1017/jog.2021.88)

Reuschen S, Xu T and Nowak W (2020) Bayesian inversion of hierarchical geostatistical models using a parallel-tempering sequential Gibbs MCMC. *Advances in Water Resources*, **141**, 103614 (doi: 10.1016/j.advwatres.2020.103614)

Reuschen S, Jobst F and Nowak W (2021) Efficient discretization-independent Bayesian inversion of high-dimensional multi-Gaussian priors using a hybrid MCMC. *Water Resources Research*, **57**(8), e2021WR030051 (doi: 10.1029/2021WR030051)

Rignot E, Mouginot J and Scheuchl B (2011) Ice flow of the Antarctic Ice Sheet. *Science*, **333**(6048), 1427–1430 (doi: 10.1126/science.1208336)

Rignot E, Mouginot J and Scheuchl B (2017) MEaSUREs InSAR-Based Antarctica ice velocity map, version 2. (doi: 10.5067/D7GK8F5J8M8R)

Rignot E, Mouginot J, Scheuchl B, van den Broeke M, van Wessem MJ and Morlighem M (2019) Four decades of Antarctic Ice Sheet mass balance from 1979–2017. *Proceedings of the National Academy of Sciences*, **116**(4), 1095–1103 (doi: 10.1073/pnas.1812883116)

Robel AA, Seroussi H and Roe GH (2019) Marine ice sheet instability amplifies and skews uncertainty in projections of future sea-level rise. *Proceedings of the National Academy of Sciences*, **116**(30), 14887–14892 (doi: 10.1073/pnas.1904822116)

Roberts GO and Sahu SK (2002) Updating schemes, correlation structure, blocking and parameterization for the Gibbs sampler. *Journal of the Royal Statistical Society: Series B (Methodological)*, **59**(2), 291–317 (doi: 10.1111/1467-9868.00070)

Roberts JL, Blankenship DD, Greenbaum JS, Beem LH, Kempf SD, Young DA, Richter TG, Van Ommen T and Le Meur E (2023) EAGLE/ICECAP II - geophysical observations (surface and bed elevation, ice thickness, gravity disturbance and magnetic anomalies) (doi: 10.26179/5xcc-4836)

Scanlan KM, Rutishauser A, Young DA and Blankenship DD (2020) Interferometric discrimination of cross-track bed clutter in ice-penetrating radar sounding data. *Annals of Glaciology*, **61**(81), 68–73 (doi: 10.1017/aog.2020.20)

Schoof C (2007) Ice sheet grounding line dynamics: Steady states, stability, and hysteresis. *Journal of Geophysical Research: Earth Surface*, **112**(F3), F03S28 (doi: 10.1029/2006JF000664)

Schroeder DM, Dowdeswell JA, Siegert MJ, Bingham RG, Chu W, MacKie EJ, Siegfried MR, Vega KI, Emmons JR and Winstein K (2019) Multidecadal observations of the Antarctic Ice Sheet from restored analog radar records. *Proceedings of the National Academy of Sciences*, **116**(38), 18867–18873 (doi: 10.1073/pnas.1821646116)

Sergienko OV and Wingham DJ (2022) Bed topography and marine ice-sheet stability. *Journal of Glaciology*, **68**(267), 124–138 (doi: 10.1017/jog.2021.79)

Seroussi H, Morlighem M, Rignot E, Larour E, Aubry D, Ben Dhia H and Kristensen SS (2011) Ice flux divergence anomalies on 79north Glacier, Greenland. *Geophysical Research Letters*, **38**(9), 2011GL047338 (doi: 10.1029/2011GL047338)

Seroussi H, Nowicki S, Simon E, Abe-Ouchi A, Albrecht T, Brondex J, Cornford S, Dumas C, Gillet-Chaulet F, Goelzer H, Golledge NR, Gregory JM, Greve R, Hoffman MJ, Humbert A, Huybrechts P, Kleiner T, Larour E, Leguy G, Lipscomb WH, Lowry D, Mengel M, Morlighem M, Pattyn F, Payne AJ, Pollard D, Price SF, Quiquet A, Reerink TJ, Reese R, Rodehacke CB, Schlegel NJ, Shepherd A, Sun S, Sutter J, Van Breedam J, van de Wal

RSW, Winkelmann R and Zhang T (2019) initMIP-Antarctica: an ice sheet model initialization experiment of ISMIP6. *The Cryosphere*, **13**(5), 1441–1471 (doi: 10.5194/tc-13-1441-2019)

Shackleton C, Matsuoka K, Moholdt G, van Liefferinge B and Paden J (2023) Stochastic simulations of bed topography constrain geothermal heat flow and subglacial drainage near Dome Fuji, East Antarctica. *Journal of Geophysical Research: Earth Surface*, **128**(11), e2023JF007269 (doi: 10.1029/2023JF007269)

Shamsipour P, Chouteau M, Marcotte D and Keating P (2010) 3D stochastic inversion of borehole and surface gravity data using geostatistics. In *EGM 2010 International Workshop*, cp–165, European Association of Geoscientists & Engineers

Siegert MJ, Ross N and Le Brocq AM (2016) Recent advances in understanding Antarctic subglacial lakes and hydrology. *Philosophical Transactions of the Royal Society A: Mathematical, Physical and Engineering Sciences*, **374**(2059), 20140306 (doi: 10.1098/rsta.2014.0306)

Sun S, Cornford SL, Liu Y and Moore JC (2014) Dynamic response of Antarctic ice shelves to bedrock uncertainty. *The Cryosphere*, **8**(4), 1561–1576 (doi: 10.5194/tc-8-1561-2014)

Teisberg TO, Schroeder DM and MacKie EJ (2021) A Machine Learning approach to mass-conserving ice thickness interpolation. In *2021 IEEE International Geoscience and Remote Sensing Symposium IGARSS*, 8664–8667 (doi: 10.1109/IGARSS47720.2021.9555002)

van Pelt WJJ, Oerlemans J, Reijmer CH, Pettersson R, Pohjola VA, Isaksson E and Divine D (2013) An iterative inverse method to estimate basal topography and initialize ice flow models. *The Cryosphere*, **7**(3), 987–1006 (doi: 10.5194/tc-7-987-2013)

van Wessem JM, van de Berg WJ, Noël BPY, van Meijgaard E, Amory C, Birnbaum G, Jakobs CL, Krüger K, Lenaerts JTM, Lhermitte S, Ligtenberg SRM, Medley B, Reijmer CH, van Tricht K, Trusel LD, van Ulft LH, Wouters B, Wuite J and van den Broeke MR (2018) Modelling the climate and surface mass balance of polar ice sheets using RACMO2 – Part 2: Antarctica (1979–2016). *The Cryosphere*, **12**(4), 1479–1498 (doi: 10.5194/tc-12-1479-2018)

Volkova A and Merkulov V (2019) Iterative approach of gravity and magnetic inversion through geostatistics. In *Petroleum Geostatistics 2019*, 1, 1–5, European Association of Geoscientists & Engineers

Weertman J (1974) Stability of the junction of an ice sheet and an ice shelf. *Journal of Glaciology*, **13**(67), 3–11 (doi: 10.3189/S0022143000023327)

Wernecke A, Edwards TL, Holden PB, Edwards NR and Cornford SL (2022) Quantifying the impact of bedrock topography uncertainty in Pine Island Glacier projections for this century. *Geophysical Research Letters*, **49**(6), e2021GL096589 (doi: 10.1029/2021GL096589)

Young DA, Wright AP, Roberts JL, Warner RC, Young NW, Greenbaum JS, Schroeder DM, Holt JW, Sugden DE, Blankenship DD, van Ommen TD and Siegert MJ (2011) A dynamic early East Antarctic Ice Sheet suggested by ice-covered fjord landscapes. *Nature*, **474**(7349), 72–75 (doi: 10.1038/nature10114)

Young DA, Schroeder DM, Blankenship DD, Kempf SD and Quartini E (2016) The distribution of basal water between Antarctic subglacial lakes from radar sounding. *Philosophical Transactions of the Royal Society A: Mathematical, Physical and Engineering Sciences*, **374**(2059), 20140297 (doi: 10.1098/rsta.2014.0297)

Zimmermann B, Zehe E, Hartmann NK and Elsenbeer H (2008) Analyzing spatial data: An assessment of assumptions, new methods, and uncertainty using soil hydraulic data. *Water Resources Research*, **44**(10), W10408 (doi: 10.1029/2007WR006604)

Zuo C, Yin Z, Pan Z, MacKie EJ and Caers J (2020) A tree-based direct sampling method for stochastic surface and subsurface hydrological modeling. *Water Resources Research*, **56**(2), e2019WR026130 (doi: 10.1029/2019WR026130)

A Markov chain Monte Carlo approach for geostatistically simulating mass conserving subglacial topography (Supplementary Materials)

Niya Shao[1], Emma Mackie[1], Michael Field[1], and Felicity McCormack[2]

[1]Department of Geological Sciences, University of Florida, Gainesville, FL, USA.
[2]Securing Antarctica's Environmental Future, School of Earth, Atmosphere and Environment, Monash University, Clayton, Kulin Nations, Victoria, Australia.

1 Quality control of bed elevation measurements via MCMC

We perform quality control on bed elevation measurements to exclude potentially erroneous data from been later used in the large-scale and small-scale chains. The quality control process is conceptually similar to large-scale chains (see the main manuscript). However, instead of strictly require preservation of bed elevation measurements, we penalize for height differences between MCMC-sampled subglacial topography and bed elevation measurements in the quality control step. Assuming independent Gaussian distribution of bed elevation error, we calculate the prior probability as below.

$$p(T) = \exp\left(-\frac{\sum(l^2)}{2\sigma_l^2}\right). \tag{s1}$$

l is the difference between the subglacial topography T and bed elevation measurements inside the high-velocity region. We only calculate l at the grid cells where bed elevation measurements are available. The standard deviation of the Gaussian distribution, σ_l, is calibrated by fitting a Gaussian distribution to the differences between BedMachine topography and bed elevation measurements. While the approximation of σ_l is not fully independent, it provides a control over the strength of bed elevation constraints, which especially useful for situations where the bed elevation measurement errors vary between different regions. We estimated the σ_l to be 100 m for Denman Glacier and 60 m for Totten Glacier. With a better quantified uncertainties in bed elevation measurements, the σ_l can possibly be determined from radar source in the future.

We use an MCMC algorithm to find bed elevation measurements that are highly incompatible with mass-conserving topographies. The MCMC iteratively proposes perturbation to the subglacial topography, searching the solution space to find topographic realizations that have small mass flux residuals while penalizing for the discrepancies with bed elevation measurements.

We start the MCMC with an initial guess of subglacial topography that has a SGS-generated topography in the slow-moving, grounded ice region, and BedMachine topography in regions classified as floating ice, open ocean, or ice-free land. The high-velocity region of the initial topography has a constant value, which is the mean of bed elevation measurements inside the high-velocity region. We iteratively update the topography inside the high-velocity region by creating blocks of spatially-correlated perturbations using random fields that are not conditioned to bed elevation measurements. These fields are sampled from zero-mean multivariate Gaussian distributions with an isotropic Gaussian covariance, which can be represented by a variogram with a zero nugget and a range sampled from a uniform distribution from 10 km to 45 km for Denman Glacier and from 10 km to 80 km for Totten Glacier. The maximum range equals the variogram range of the bed elevation measurements, and the minimum range helps to generate topographic features with relatively shorter wavelength, which we kept to be larger than 10 km. The amplitude of the generated field is drawn uniformly between 50 to 200 m for Denman and between 50 to 150 m for Totten, which we tuned for an acceptance rate between 0.1 and 0.4. In addition, we utilize the block-update similar to large-scale chain for increasing the acceptance rate and facilitate chain convergence. The lateral dimensions of the block are drawn from a uniform distribution from 50 km to 200 km to ensure an acceptance rate between 0.1 and 0.4. Outside the high-velocity region, the perturbations are masked out, and the topography remain to be the SGS-generated initial topography.

The nature of the random field perturbation indicates that the proposal distribution is symmetric ($q(T'|T) = q(T|T')$). The random fields used for perturbing topography are sampled from a multivariate Gaussian distribution with zero mean. The random field used to obtain T' from T is exactly the random field used to obtain T from T' with an opposite sign, which has the same probability of being generated. With the definition of $p(T)$ and the symmetric proposal distribution, the acceptance rate in the step 3 of MCMC algorithm (Method - Bayes' Theorem and MCMC subsection) for the data quality control step is calculated as.

$$\begin{aligned}\alpha(x,y) &= \min\left[\frac{p(T')p(d|T')}{p(T_{i-1})p(d|T_{i-1})}, 1\right] \\ &= \min\left[\exp\left(-\frac{\sum(r'^2)-\sum(r_{i-1}^2)}{2\sigma_r^2} - \frac{\sum(l'^2)-\sum(l_{i-1}^2)}{2\sigma_l^2}\right), 1\right].\end{aligned} \tag{s2}$$

The iterative random field perturbation does not constrain the roughness of the subglacial topography, which leads to the possibility of overfitting the topography to mass flux residuals. We stopped the MCMC at the iteration when (1) the differences between the MCMC-sampled subglacial topography and bed elevation measurements stabilize and (2) 85% of the bed elevation measurements that will be excluded (which are higher than MCMC-sampled topography by more than 1.5 standard deviations of l) does not change across more than a hundred thousands iterations. We stopped the MCMC at 500,000th iteration for Denman Glacier and at 800,000th iterations for Totten Glacier. The last 5000 subglacial topographies sampled by the chains are provided to quality control the bed elevation measurements. We remove bed elevation measurements that are 1.5 standard deviations shallower than the mean topography of the last 5000 iterations.

2 Data Quality Control Results

Fig. S1 presents results of the quality control step for Denman Glacier. In Fig. S1a, most of discrepancy to bed elevation measurements occurred inside the Denman trough. While the simulated subglacial topography is shallower than bed elevation measurements at locations upstream and downstream of the trough, this topography is deeper than the measurements at middle segment of the trough. The overall result reconstruct a trough shallower than the trough reconstructed in BedMachine (Morlighem and others, 2020). The results shows a high inconsistency among bed elevation measurements in the trough.

Fig. S2 presents the result of quality control step for Totten Glacier. The quality control process clearly captured a radar segment (enclosed by a blue circle) near easting $\sim 2250km$ and northing $\sim -1000km$, where the simulated subglacial topography is much lower than the bed elevation measurements. This radar segment also has high cross-sectional errors with surrounding bed elevation measurements, which further suggests existing data errors. At other locations, the difference between simulated subglacial topography and the bed elevation measurements are generally small, which only cause several sporadic bed elevation measurements to be excluded from the dataset.

We calculate the standard deviation of the elevation differences between the subglacial topography sampled from the MCMC in the quality control step and the bed elevation measurements. We identify locations where bed elevation measurements is at least 1.5 standard deviation shallower than the generated topography. For Denman region, we additionally select 10 grid cells in the vicinity of the Denman trough, which could potentially be corrupted by clutter. In total, 59 grid cells – highlighted in red in Fig. S1(b) – are excluded from the bed elevation measurements in Denman. For Totten region, we observe that bed elevation measurements from one radar flight line have large cross-section errors with other bed elevation measurements. We exclude additional 169 grid cells of bed elevation measurements on this flight line. In total, 680 grid cells are excluded from the bed elevation measurements in Totten (Fig. S1(d)).

3 Distribution of mass flux residuals

Mass flux residuals represent the spurious ice flux that arises when combining observed velocity with interpolated subglacial topography. In the context of known subglacial topography, the mass flux residuals are caused by uncertainties in ice velocities, surface mass balance, and surface elevation change. These data uncertainties could rises from the observational error, the coarse spatial resolution, and the asynchronous data collection time. However, because the topography is not known, we approximate the distribution of mass flux residuals using BedMachine.

BedMachine estimate mass-conserving topography by finding a ice velocity v_x, v_y within a bound around ice surface velocity v_{sx}, v_{sy} ($v_x = \alpha_1 v_{sx} + \alpha_2, \alpha_1 \in [0.95, 1], \alpha_2 \in [-50, 50]$, and similar for v_y), such that the subglacial topography solution has minimized discrepancy with bed elevation measurements and minimized gradients (Morlighem and others, 2011). Mass flux residuals of BedMachine topography then arise from the incompatibility between observed surface velocity v_{sx}, v_{sy} and topography estimated from optimized velocity v_x, v_y.

To confirm the validity of mass flux residuals estimated from BedMachine, we calculate mass

flux residuals on densely-measured subglacial topographies under Pine Island Glacier (Bingham and others, 2017) (Fig. S3). The mass flux residual distributions defined for Denman and Totten are shown to be within the plausible range of distribution.

4 Weighted Random Field Calculations

In the large-sale chains, blocks of weighted random fields iteratively update the topography while preserving bed elevation measurements and avoiding sharp changes in subglacial topography. We generate the weighted random fields by multiplying a random field with the data weight matrix and the edge weight matrix.

The data weights matrix $W(\boldsymbol{d}, d_{max})$ helps to avoid perturbations at grid cells with bed elevation measurements. $W(\boldsymbol{d}, d_{max})$ has the size of the random field. $\boldsymbol{d}$ denotes the distance between a grid cell and its closest bed elevation measurements. d_{max} denotes the maximum correlation length, which is set to the range of the empirical variogram of the bed elevation measurements. For Denman, $d_{max} = 45km$, and for Totten, $d_{max} = 80km$. We denote every entry in $W(\boldsymbol{d}, d_{max})$ as $w_{i,j}(d_{i,j}, d_{max})$, where $d_{i,j}$ represent $\boldsymbol{d}$ at the (i, j) grid cell. We use a logistic function (Equation s3) to calculate $w_{i,j}$ such that $W(\boldsymbol{d}, d_{max})$ has 0 at locations of bed elevation measurements and gradually change to 1 at location at least d_{max} away from any bed elevation measurements.

$$
\begin{aligned}
d_n(d_{i,j}, d_{max}) &= \begin{cases} 1, & \text{if } d_{i,j} \geq d_{max} \\ \frac{d_{i,j}}{d_{max}}, & \text{otherwise} \end{cases} \\
w_{i,j}(d_{i,j}, d_{max}) &= \left(\frac{2}{1 + \exp(-6 d_n(d_{i,j}, d_{max}))}\right) - 1
\end{aligned}
\tag{s3}
$$

In addition, the edge weights matrix $K(\boldsymbol{s}, d_{max})$ prevents sudden change at the edge of the random field block when adding the block to topography. $K(\boldsymbol{s}, d_{max})$ is calculated using the same logistic function but with $\boldsymbol{d}$ replaced by $\boldsymbol{s}$ (Equation s4), which is the distances of a grid cell to the closest edge of the update block. The weight gradually changes from 0 at the edges to 1 at locations that are at least d_{max} away from the edges. In the following equation, $s_{i,j}$ represents $\boldsymbol{s}$ at (i, j) grid cell, and $k_{i,j}$ represent entries of K.

$$
\begin{aligned}
d_n(s_{i,j}, d_{max}) &= \begin{cases} 1, & \text{if } s_{i,j} \geq d_{max} \\ \frac{s_{i,j}}{d_{max}}, & \text{otherwise} \end{cases} \\
k_{i,j}(s_{i,j}, d_{max}) &= \left(\frac{2}{1 + \exp(-6 d_n(s_{i,j}, d_{max}))}\right) - 1
\end{aligned}
\tag{s4}
$$

Multiplying the data weight matrix and the edge weight matrix with the random field ensures that the resulting weighted random field changes smoothly from 0 at bed elevation measurements locations and blocks edges to the random field's values elsewhere.

5 Large-scale chains burn-in period and sampling rate

We use trace plot to determine when to start sampling subglacial topographies from the large-scale chains. MCMC method often requires a period of initialization (a.k.a. burn-in) when subglacial topography is iteratively updated from the initial guess to a different configuration that produces low mass flux residuals. Without this burn-in period, subglacial topography samples generated by MCMC might still be under the influence of the initial guess. We use trace plot to determine the burn-in period. We apply a Gaussian smooth filter with a kernel size of 5 km to the subglacial topography at each iteration to obtain large-scale topographic features. We then record bed elevation of the smoothed subglacial topography at grid cells marked on Fig. S5a. These 200 grid cells are randomly selected from all grid cells in the high-velocity region. We observe that the values of the smoothed topographies stabilize before the 200,000 iterations for Denman Glacier and 600,000 iterations for Totten Glacier. We discard all topography samples generated before 200,000 iterations for Denman Glacier and 600,000 iterations for Totten Glacier.

We use autocorrelation to determine the number of iterations between each topography samples obtained from the large-scale chain. The subglacial topographies generated by MCMC are correlated among neighboring iterations. Only when two topographies are separated by enough iterations, they can be considered as pseudo-independent samples. Auto-correlation plots have often been used to determine this separating interval (Jones and Qin, 2022). Fig. S6 showcases the autocorrelations of individual grid cells in a large-sale chain for Denman Glacier, whereas Fig. S7 plots autocorrelations for Totten Glacier. We choose the separating interval by the distance where the autocorrelations dropped below ~ 0.25, which is 4,000 iterations for Denman Glacier and 30,000 iterations for Totten Glacier.

6 Subglacial topography profile across Denman Trough

We plot additional cross sections across the Denman trough to show the differences between SGS-generated subglacial topographies (S8a) and MCMC-generated subglaical topographies (S8b).

References

Bingham RG, Vaughan DG, King EC, Davies D, Cornford SL, Smith AM, Arthern RJ, Brisbourne AM, De Rydt J, Graham AGC, Spagnolo M, Marsh OJ and Shean DE (2017) Diverse landscapes beneath Pine Island Glacier influence ice flow. *Nature Communications*, **8**(1), 1618 (doi: 10.1038/s41467-017-01597-y)

Jones GL and Qin Q (2022) Markov Chain Monte Carlo in practice. *Annual Review of Statistics and Its Application*, **9**(1), 557–578 (doi: 10.1146/annurev-statistics-040220-090158)

Morlighem M, Rignot E, Seroussi H, Larour E, Ben Dhia H and Aubry D (2011) A mass conservation approach for mapping glacier ice thickness. *Geophysical Research Letters*, **38**(19), L19503 (doi: 10.1029/2011GL048659)

Morlighem M, Rignot E, Binder T, Blankenship D, Drews R, Eagles G, Eisen O, Ferraccioli F, Forsberg R, Fretwell P, Goel V, Greenbaum JS, Gudmundsson H, Guo J, Helm V, Hofstede C, Howat I, Humbert A, Jokat W, Karlsson NB, Lee WS, Matsuoka K, Millan R, Mouginot J, Paden J, Pattyn F, Roberts J, Rosier S, Ruppel A, Seroussi H, Smith EC, Steinhage D, Sun B, van den Broeke MR, van Ommen TD, van Wessem M and Young DA (2020) Deep glacial troughs and stabilizing ridges unveiled beneath the margins of the Antarctic ice sheet. *Nature Geoscience*, **13**(2), 132–137 (doi: 10.1038/s41561-019-0510-8)

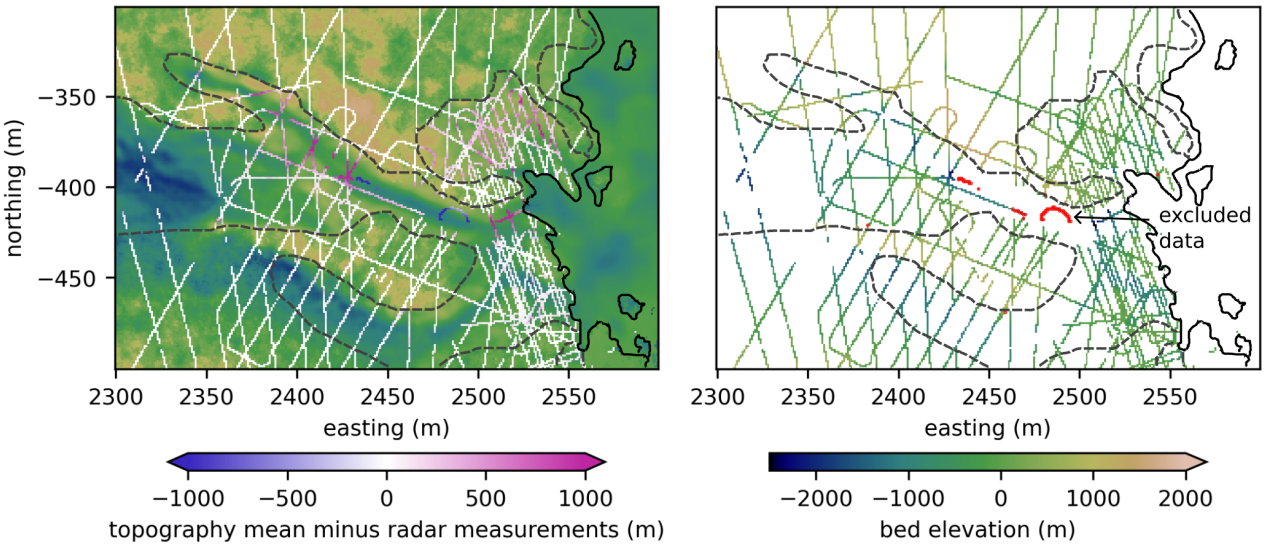

Figure S1: This figure shows the result of quality control step for Denman Glacier. Left subplot shows the differences between topography generated from the MCMC algorithm in the quality control step and the bed elevation measurements, which is overlaid upon the subglacial topography generated in MCMC after burn-in period. Right subplot shows the bed elevation measurements, where the locations of excluded bed elevation measurements are highlighted in red

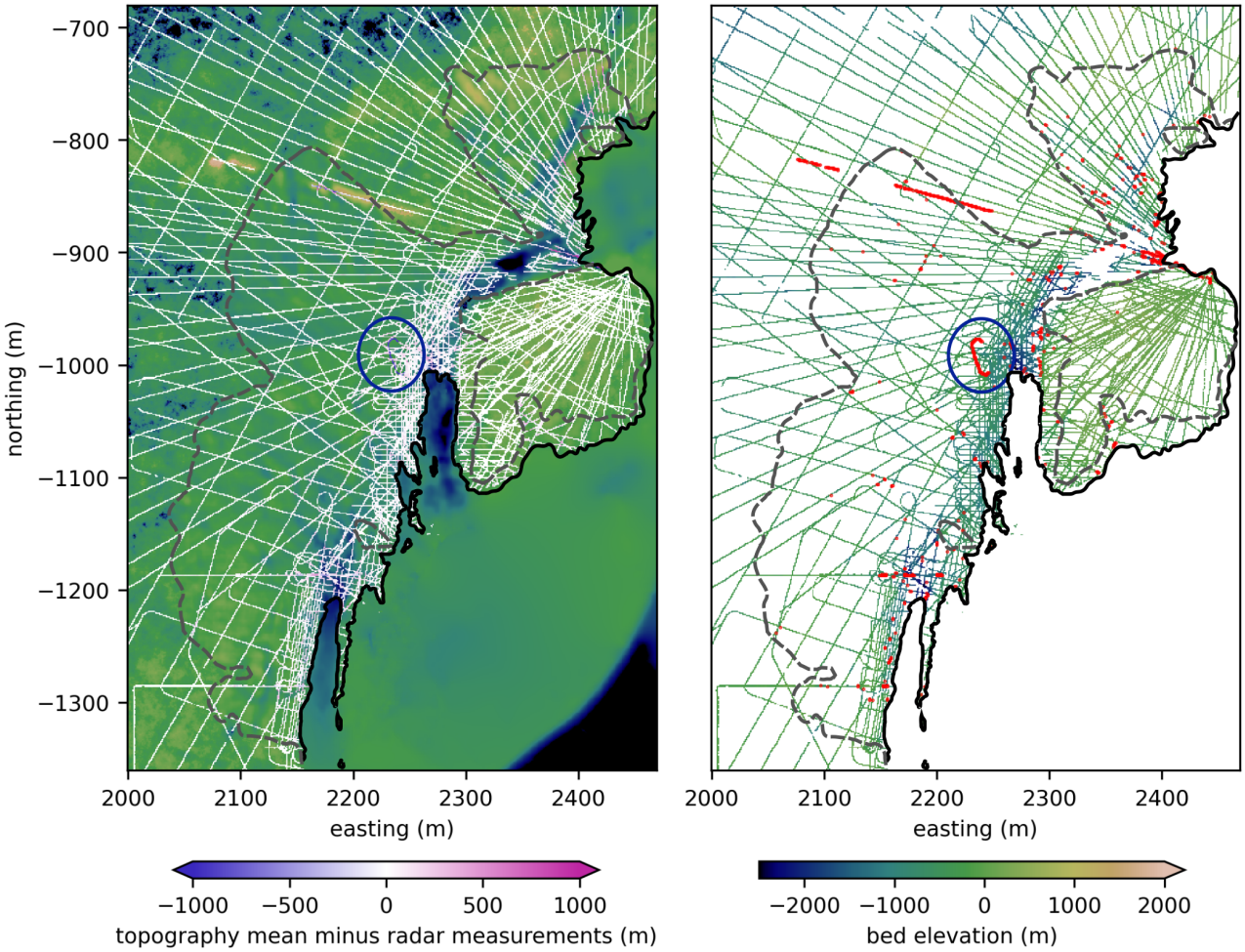

Figure S2: This figure shows data similar to Fig. S1 but for Totten Glacier. The left subplot shows the differences between topography generated from the MCMC algorithm in the quality control step and the bed elevation measurements, which is overlaid upon the subglacial topography generated in MCMC after burn-in period. The right subplot shows the bed elevation measurements, where the locations of excluded bed elevation measurements are highlighted in red. The blue circle is a reference to a radar segment that have large errors.

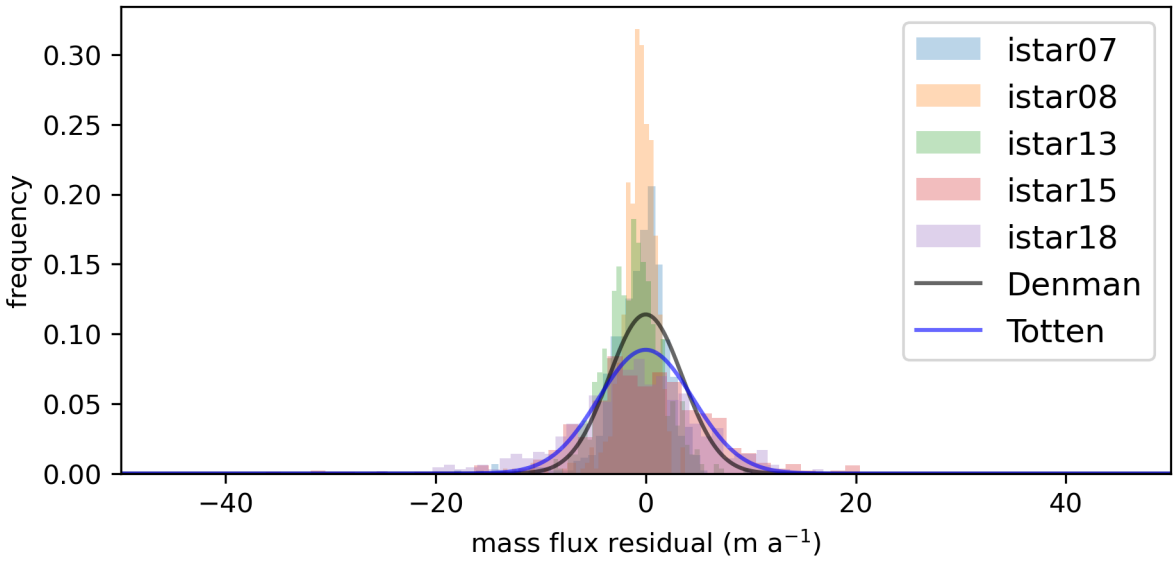

Figure S3: The figure shows histograms of mass flux residuals calculated from regions of densely-measured subglacial topography (Bingham and others, 2017). The datasets used for calculating mass flux residuals are described in the Study Region & Data section of the manuscript. The mass flux residual histograms are overlapped with the mass flux residual distributions approximated from BedMachine (Morlighem and others, 2020) for Denman and Totten Glaciers.

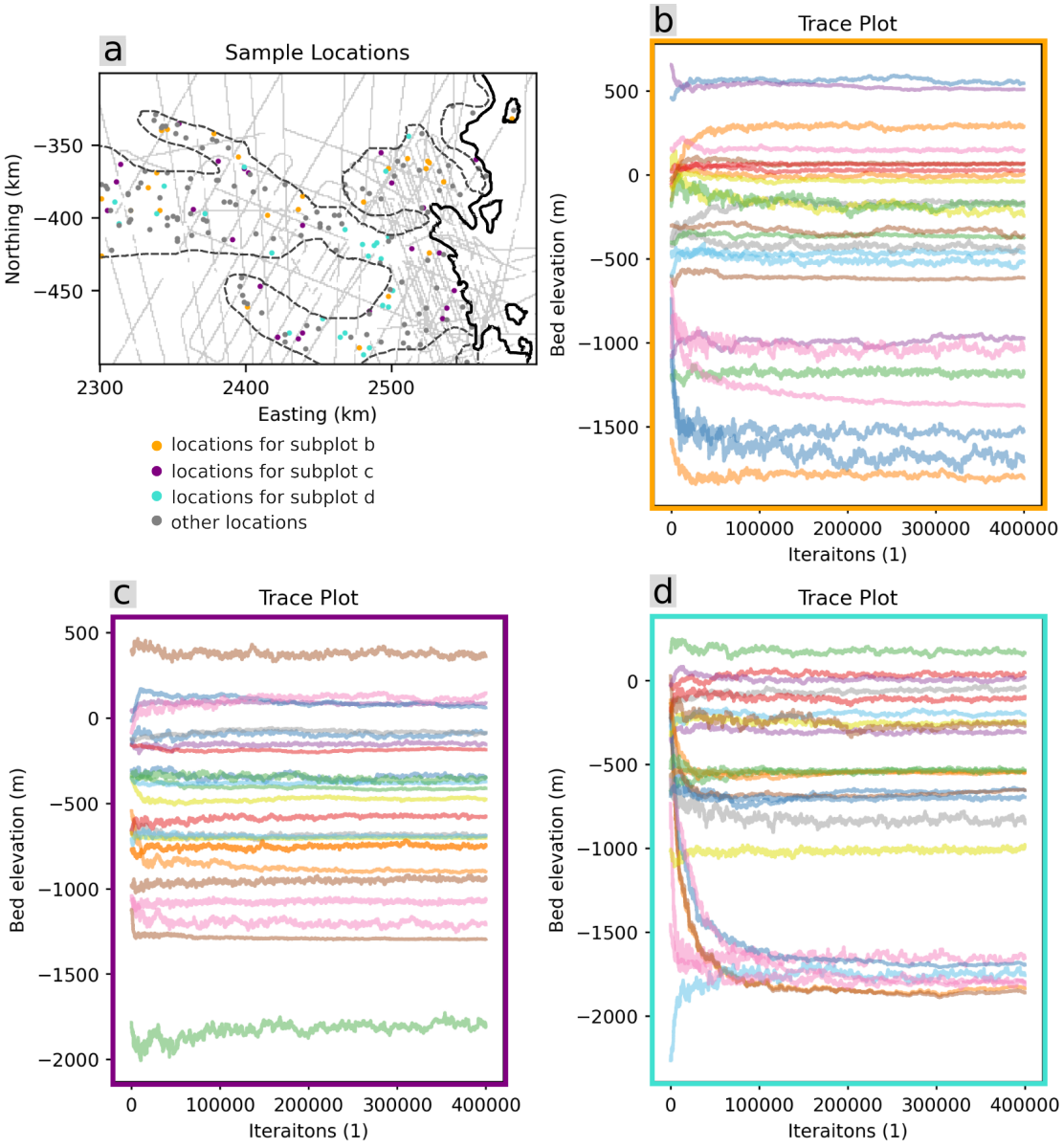

Figure S4: This figures shows bed elevation values at randomly chosen grid cells of Denman Glacier in a large-scale chain. Subplot a shows the location of the randomly chosen grid cells, with orange marks indicating locations used to generate b, purple marks for c, and green marks for d. Subplots b, c, and d show the trace plots of bed elevation from iteration 0 to 400,000 at their respective grid cells for the large-scale chain.

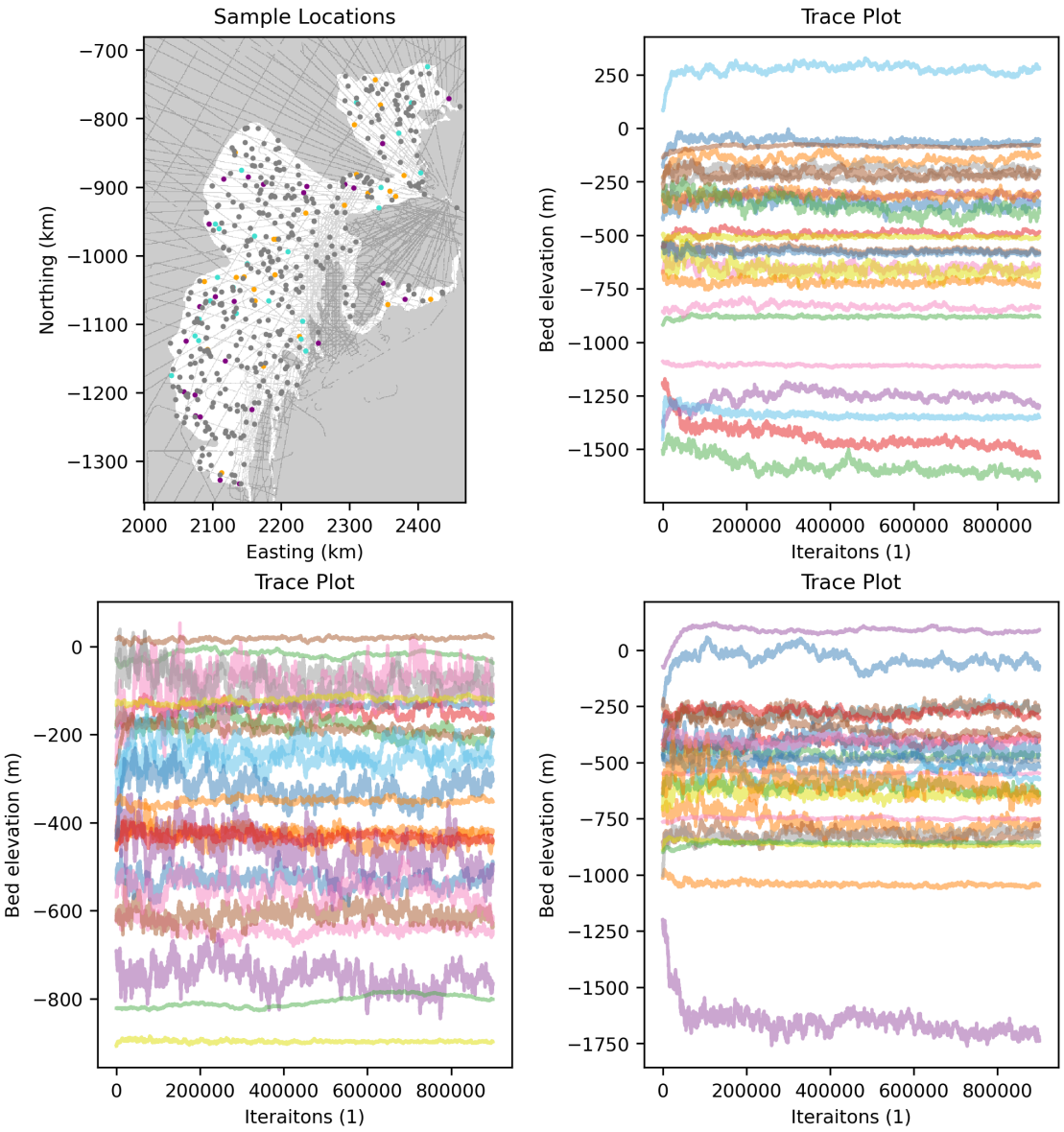

Figure S5: This figures shows similar data as Fig. 4 but for Totten Glacier. Subplot a shows the location of the randomly chosen grid cells, with orange marks indicating locations used to generate b, purple marks for c, and green marks for d. Subplots b, c, and d show the trace plots of bed elevation from iteration 0 to 800,000 at their respective grid cells for the large-scale chain.

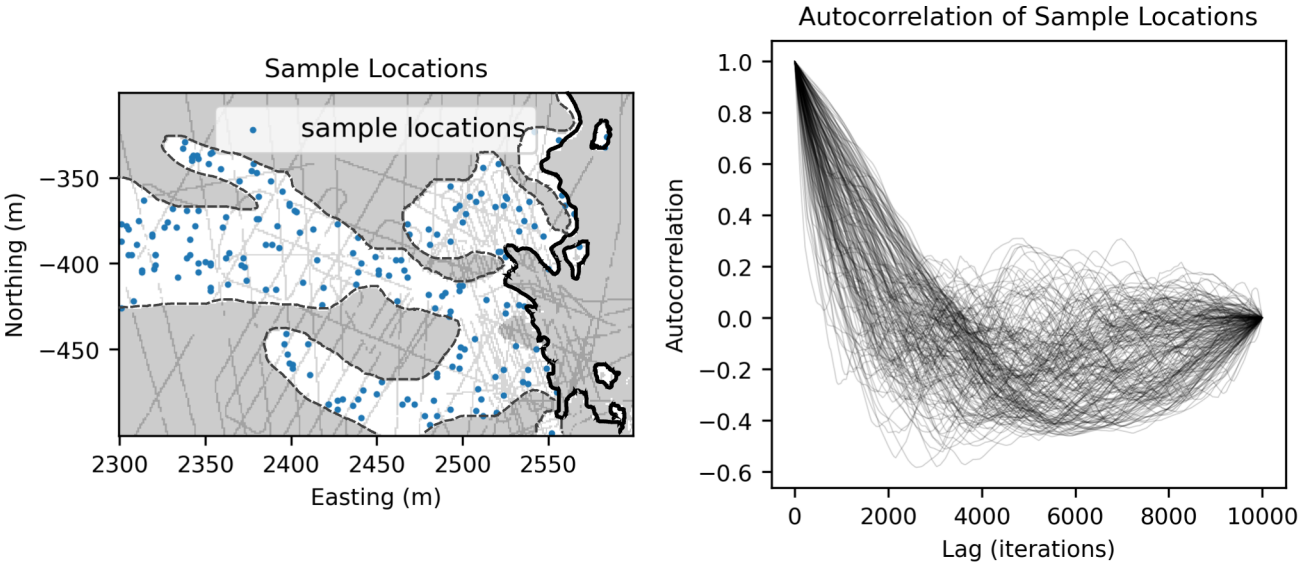

Figure S6: This figure shows autocorrelation of individual grid cells during a large-scale chain for Denman Glacier. Subplot a presents the high velocity region (light gray, enclosed by dashed gray lines), the location of bed elevation measurements (semi-transparent white), the grounding line (black lines), and the locations where we calculate autocorrelations (blue dots). Subplot b plots the autocorrelations of 200 grid cells in a large-scale chains from iteration 200,000 to iteration 210,000.

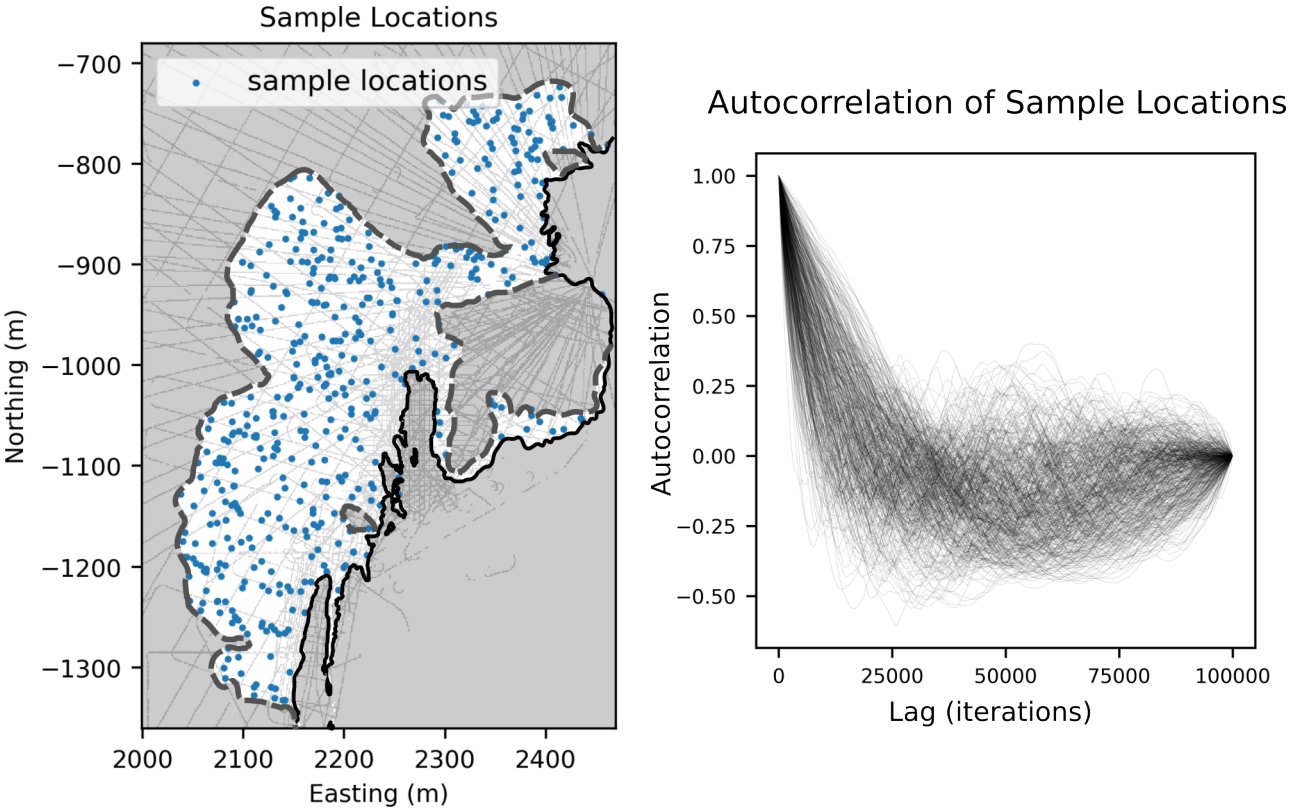

Figure S7: This figure shows autocorrelation of individual grid cells during a large-scale chain for Totten Glacier. Subplot a presents the high velocity region (light gray, enclosed by dashed gray lines), the location of bed elevation measurements (semi-transparent white), the grounding line (black lines), and the locations where we calculate autocorrelations (blue dots). Subplot b plots the autocorrelations of 200 grid cells in a large-scale chains from iteration 600,000 to iteration 700,000.

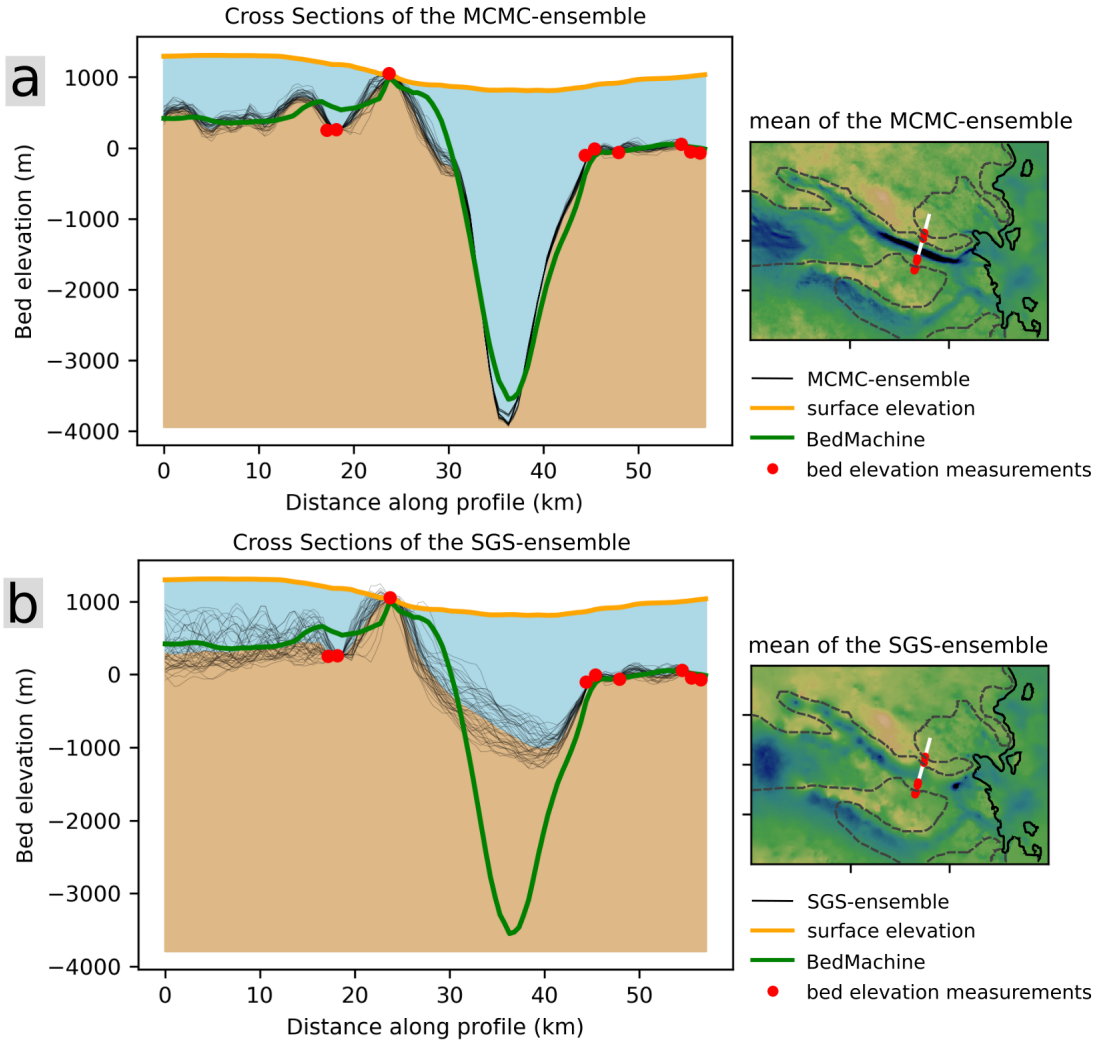

Figure S8: The cross section of subglacial topographies generated by the mass-conserving MCMC approach and by SGS. The left column shows cross sections of 40 subglacial topographies generated by the geostatistical MCMC (a) and SGS (b). The right column shows location of the cross sections, where the base map is mean of the subglacial topography ensemble generated by geostatistical MCMC (a) or SGS (b), and the white lines denote location of the cross section.